iScience

CellPress

Article

Toward a Low-Cost Alkaline Zinc-Iron Flow Battery with a Polybenzimidazole Custom Membrane for Stationary Energy Storage

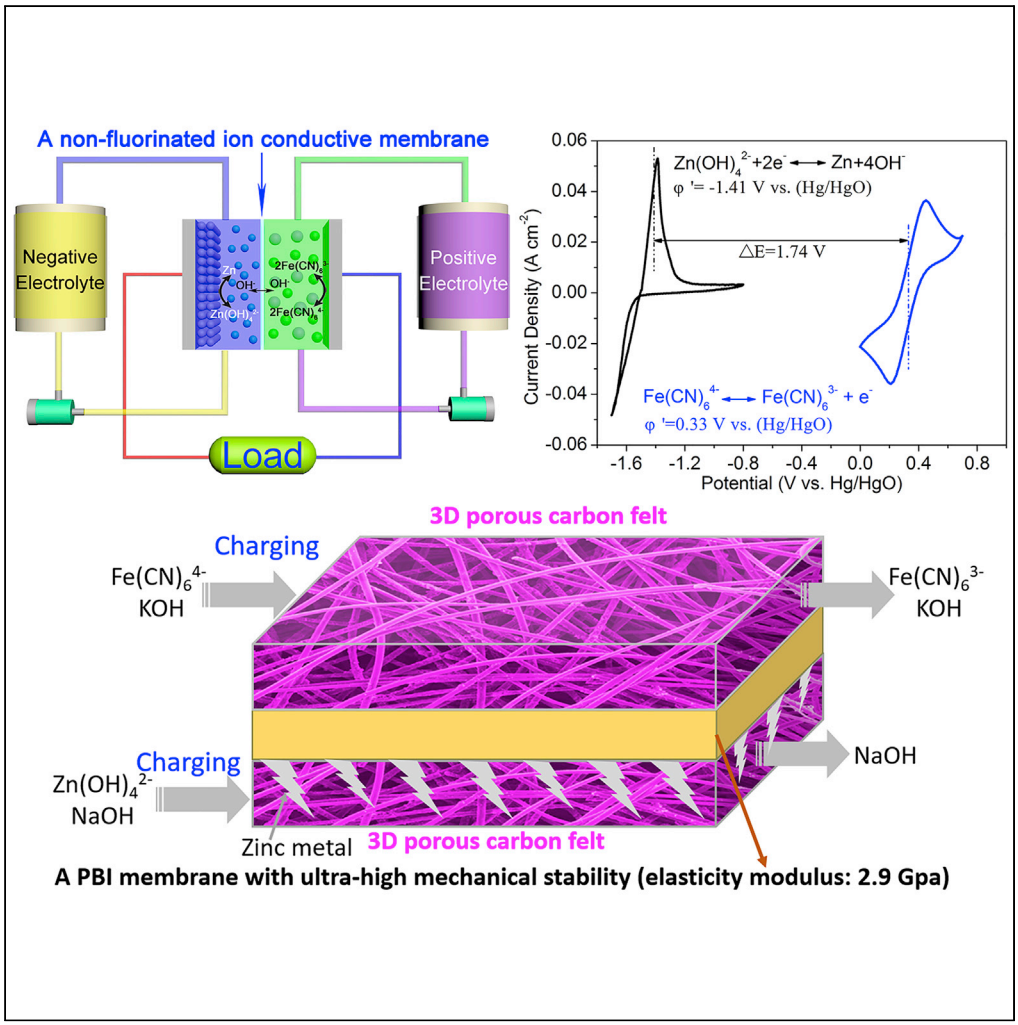

Zhizhang Yuan, Yinqi Duan, Tao Liu, Huamin Zhang, Xianfeng Li

lixianfeng@dicp.ac.cn

HIGHLIGHTS

An alkaline zinc-iron flow battery is presented for stationary energy storage

A battery with self-made membrane shows a CE of 99.49% and an EE of 82.78% at 160 mA cm^{-2}

The self-made membrane shows excellent mechanical and chemical stability

A kilowatt cell stack with a capital cost under $90/kWh has been demonstrated

Yuan et al., iScience 3, 40–49
May 25, 2018 © 2018 The Author(s).
https://doi.org/10.1016/j.isci.2018.04.006

iScience

CellPress

Article

Toward a Low-Cost Alkaline Zinc-Iron Flow Battery with a Polybenzimidazole Custom Membrane for Stationary Energy Storage

Zhizhang Yuan,[1,3] Yinqi Duan,[1,3] Tao Liu,[1] Huamin Zhang,[1,2] and Xianfeng Li[1,2,4,*]

SUMMARY

Alkaline zinc-iron flow battery is a promising technology for electrochemical energy storage. In this study, we present a high-performance alkaline zinc-iron flow battery in combination with a self-made, low-cost membrane with high mechanical stability and a 3D porous carbon felt electrode. The membrane could provide high hydroxyl ion conductivity while resisting zinc dendrites well owing to its high mechanical stability. The 3D porous carbon felt could serve as a guidance for the zinc stripping/plating, which can effectively suppress zinc dendrite/accumulation as well. Thus this battery demonstrates a coulombic efficiency of 99.5% and an energy efficiency of 82.8% at 160 mA cm^{-2}, which is the highest value among recently reported flow battery systems. The battery can stably run for more than 500 cycles, showing very good stability. Most importantly, the practicability of this battery is confirmed by assembling a kilowatt cell stack with capital cost under $90/kWh.

INTRODUCTION

Flow batteries are of tremendous importance for their application in increasing the quality and stability of the electricity generated by renewable energies like wind or solar power (Yang et al., 2011; Dunn et al., 2011). However, research into flow battery systems based on zinc/bromine, iron/chromium, and all-vanadium redox pairs, to name but a few, has encountered numerous problems, such as the corrosion of bromine, poor kinetics of Cr^{2+}/Cr^{3+} redox pair, relatively high cost, and low energy density of all-vanadium redox pairs, although these battery systems are currently at the demonstration stage (Yuan et al., 2016b; Park et al., 2016). These barriers have, on the one hand, hindered their further wide scale deployment, and on the other hand, accelerated research efforts into new flow battery chemistries (or the next-generation flow batteries, aqueous or non-aqueous redox flow batteries) (Perry and Weber, 2015; Park et al., 2016). Among the reported new systems, non-aqueous redox flow battery systems, having the features of wide electrochemical window, high energy density, inexpensive redox active materials, etc., are currently at the proof-of-concept stage. However, the low concentration and poor ion conductivity of organic-based electrolytes are the most critical issues to overcome (Park et al., 2016). Although aqueous flow battery systems, like TEMPO (2,2,6,6-tetramethylpiperidine-1-oxyl)-based flow battery and quinone-based flow battery, have been successfully demonstrated at the laboratory scale (the electrode area is normally less than 10 cm^2), their relatively low performance at high current density (normally less than 100 mA cm^{-2}, when the energy efficiency [EE] was above 80%) (Liu et al., 2016; Wang et al., 2016; Janoschka et al., 2015, 2016; Winsberg et al., 2016; Hu et al., 2017) limits the quick response for energy conversion and increases the integration cost. In addition, some of the systems still have low open cell voltage (OCV) or low electrolyte concentration. The low working current density together with the low OCV will result in low power density of a flow battery, further leading to an increased stack size and an overall increased capital cost of a flow battery system. Currently, only a few membrane materials (such as perfluorinated ion-exchange membranes because of their high stability in critical medium, e.g., strongly acidic or alkaline conditions and highly oxidative medium) have been considered (Gong et al., 2015, 2016; Wang et al., 2011; Li et al., 2015, 2016; Lin et al., 2015, 2016; Orita et al., 2016), which will definitely further result in cost issue for battery stacks (Chu et al., 2017). Besides, upscaling for practical application of these newly developed aqueous flow battery systems have been rarely reported, which may induce limitations on the energy storage system development to some extent.

The alkaline zinc ferricyanide flow battery owns the features of low cost and high voltage together with two-electron-redox properties, resulting in high capacity (McBreen, 1984; Adams et al., 1979; Adams, 1979). The alkaline zinc ferricyanide flow battery was first reported by G. B. Adams et al. in 1981; however,

[1]Division of Energy Storage, Dalian Institute of Chemical Physics, Chinese Academy of Sciences, 457 Zhongshan Road, Dalian 116023, P. R. China

[2]Collaborative Innovation Center of Chemistry for Energy Materials (iChEM), Dalian 116023, P. R. China

[3]These authors contributed equally

[4]Lead Contact

*Correspondence: lixianfeng@dicp.ac.cn

https://doi.org/10.1016/j.isci.2018.04.006

 © 2018 The Author(s).
This is an open access article under the CC BY-NC-ND license (http://creativecommons.org/licenses/by-nc-nd/4.0/).

further work on this type of flow battery has been broken off, owing to its very poor cycle life and the relatively low operating current density (35 mA cm^{-2}) (McBreen, 1984). The poor cycle life is mainly due to the zinc dendrite under alkaline medium, where a cadmium-plated (Zn- or Cu-plated) iron substrate was employed for zinc stripping/plating, while the low operating current density could be due to the high resistance of a cation-conducting membrane and severe zinc dendrite derived from the metal electrode.

Here we present a long cycle life alkaline zinc-iron flow battery with a very high performance. The battery employs $Zn(OH)_4^{2-}$/Zn and $Fe(CN)_6^{3-}$/$Fe(CN)_6^{4-}$ as the negative and positive redox couples, respectively, while a self-made, cost-effective polybenzimidazole (PBI) membrane and a 3D carbon felt electrode were combined. The PBI membrane carrying heterocyclic rings can guarantee fast transportation of hydroxyl ions after doping with a base solution (Li et al., 2003; Yuan et al., 2016a). Most importantly, the PBI membrane with ultra-high mechanical stability can resist the zinc dendrite very well, which ensures the cycling stability of the alkaline zinc-iron flow battery. In addition, a 3D porous carbon felt with high porosity and surface area, which serves as guidance for the zinc stripping/plating and suppresses zinc dendrite/accumulation effectively, provides the battery with excellent cycling stability and rate performance. Moreover, the concentration of $Fe(CN)_6^{3-}$/$Fe(CN)_6^{4-}$ redox couple can reach 1 mol L^{-1} by optimizing the composition of electrolyte, which is much higher than the reported concentration of this redox couple (0.4 mol L^{-1}) (Orita et al., 2016; Lin et al., 2015, 2016; Selverston et al., 2016, 2017). The high concentration of active materials thus can afford the battery with high energy density. As a result, the proposed zinc-iron flow battery demonstrated an EE of 82.78% even at a high current density of 160 mA cm^{-2}. A charge/discharge experiment of 500 cycles further confirmed the excellent stability of this system.

RESULTS AND DISCUSSION

Electrochemical Performance of the Alkaline Zinc-Iron Flow Battery Using a PBI Membrane and a 3D Porous Carbon Felt Electrode

Figure 1A showed the principle and structure of the reported alkaline zinc-iron flow battery, where $Zn(OH)_4^{2-}$/Zn pair served as the negative active material and $Fe(CN)_6^{3-}$/$Fe(CN)_6^{4-}$ pair was employed as a positive redox couple. For batteries involving stripping/plating process, especially for Li- and zinc-based batteries, a membrane with high mechanical stability is always in high demand (Figure 1C), since it can effectively suppress dendritic growth during metal plating (Li or zinc), whose safety issues upon internal short circuit could be mitigated. A PBI membrane (Figure S1), which is widely used in fuel cells because of its very high chemical and mechanical stability (the elasticity modulus of the PBI was higher than 2.9 GPa, Figure S2), along with very high thermal stability, was used as the separator. Carrying heterocyclic rings, a PBI membrane can guarantee the fast transportation of hydroxyl ions after doping with a base solution (Figure 1D). For comparison, a Nafion (Nafion 115, whose elasticity modulus was about 94 MPa, Figure S2) membrane, which was widely used in aqueous flow battery systems, even in the alkaline medium, was used as a reference.

The cyclic voltammetry (CV) of the two redox pairs on a graphite plate working electrode at a scan rate of 40 mV s^{-1} (Figure 1B) predicts an equilibrium formal potential of 1.74 V, which corresponds to the redox reactions $Fe(CN)_6^{3-}$/$Fe(CN)_6^{4-}$ at the positive side and $Zn(OH)_4^{2-}$/Zn at the negative side. CV curves at different scan rates ranging from 10 mV s^{-1} to 60 mV s^{-1} reveal that $Fe(CN)_6^{3-}$/$Fe(CN)_6^{4-}$ redox reaction is a standard diffusion-controlled process (Figure S3A). Based on the Randles-Sevcik equation, the diffusion coefficients of $Fe(CN)_6^{3-}$ and $Fe(CN)_6^{4-}$ in the alkaline electrolyte were found to be 9.03×10^{-6} cm^2 s^{-1} and 8.19×10^{-6} cm^2 s^{-1}, respectively, calculating from the linear ip-$v^{1/2}$ relationship (Figure S3B). The CV of $Zn(OH)_4^{2-}$/Zn exhibits a different behavior on the electrode (Figures S3C and S3D), where both a surface-reaction-controlled process (linear dependence, $ip \propto v$) and a diffusion-controlled process can be distinguished (Cheng et al., 2013). For better understanding the process of zinc deposition, a rotating disk electrode (RDE) technique was employed (Figure S4), demonstrating a diffusion-controlled process.

An alkaline zinc-iron flow battery is displayed in Figure S5. Solutions of 0.3 mol L^{-1} $Zn(OH)_4^{2-}$ and 0.6 mol L^{-1} $K_4Fe(CN)_6$ in 5 mol L^{-1} NaOH were used as negative and positive electrolytes, respectively. A self-made PBI membrane with an active area of 48 cm^2 was employed in the structure. The battery was charged and discharged at a constant current density of 80 mA cm^{-2}, affording a specific discharging capacity of 10.66 Ah L^{-1} with a starting discharging voltage of 1.82 V (Figure S6A). This high starting

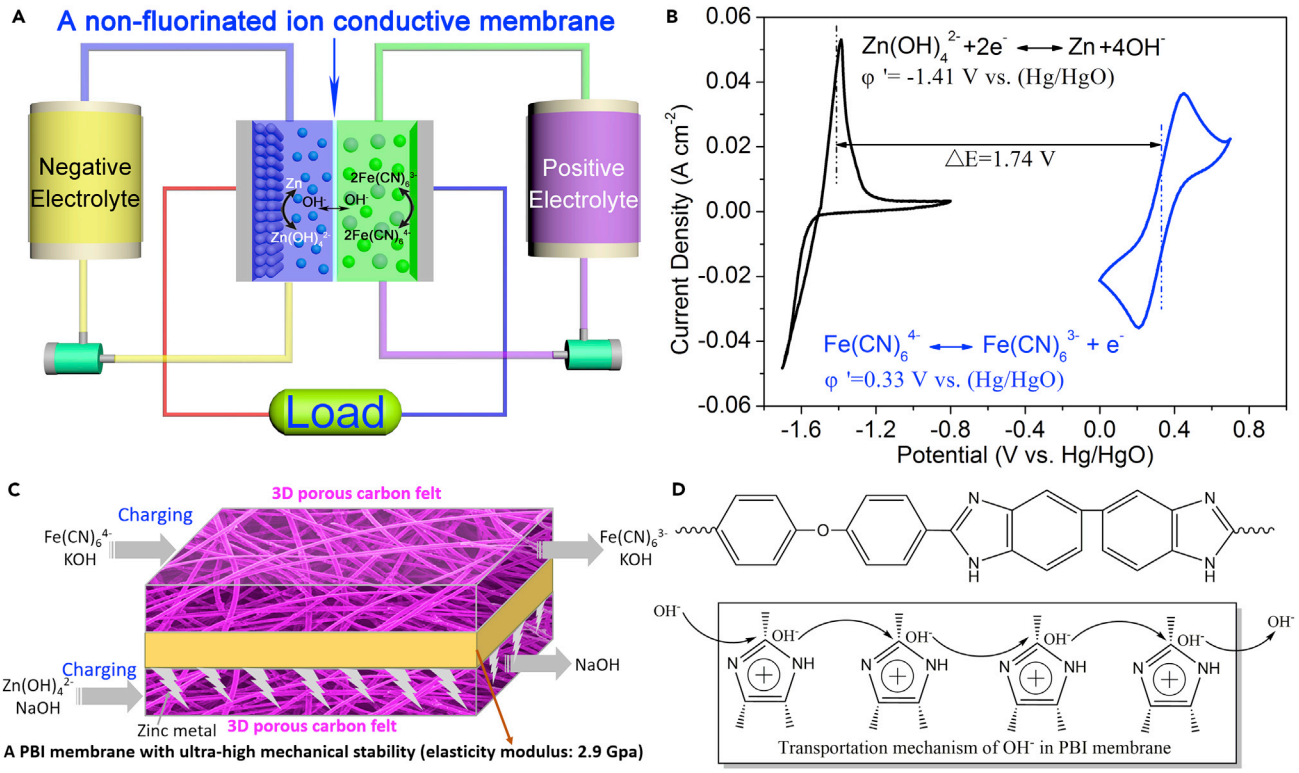

Figure 1. The Utilization of an Alkaline Zinc-Iron Flow Battery Using a Self-made, Low-Cost Non-fluorinated Ion-Exchange Membrane

(A) Schematic of the alkaline zinc-iron flow battery.

(B) Cyclic voltammetry of negative and positive redox pairs in sodium hydroxide solution. The negative electrolyte contains 0.1 mol L^{-1} $Zn(OH)_4^{2-}$ and 3 mol L^{-1} sodium hydroxide solution; the positive electrolyte contains 0.2 mol L^{-1} $K_3Fe(CN)_6$, 0.2 mol L^{-1} $K_4Fe(CN)_6$, and 3 mol L^{-1} sodium hydroxide solution. The working electrode is graphite plate, and the scan rate is 40 mV s^{-1}.

(C) Schematic of introjecting a PBI membrane with ultra-high mechanical stability and a 3D porous carbon felt for an alkaline zinc-iron flow battery.

(D) The transportation mechanism of OH^- in a PBI membrane.

See also Figures S1–S4, S8–S16, S18, S20, and S21.

discharging voltage is unprecedented among all recently reported flow battery systems. The charge and discharge curves are given in Figure S6A. The battery exhibited an electrolyte utilization of 66% at a theoretical capacity of 16.07 Ah L^{-1}, along with a coulombic efficiency (CE) of 99.97%, an EE of 88.07%, and a voltage efficiency (VE) of 88.11%. A permeability experiment of anionic active species through the PBI membrane was carried out to further verify the high selectivity of the membrane. As expected, the PBI membrane demonstrates an ultra-high selectivity for both positive and negative active species (Figure S7), which contributes to the high CE of the battery.

To confirm the reliability and practicality of the alkaline zinc-iron flow battery, the cycle performance was measured at a current density of 60 mA cm^{-2}. An outstanding cycling stability with nearly 100% capacity retention can be obtained over more than 500 cycles with an over 99% CE and a nearly 90% EE (Figure S6B), indicating the high reversibility of $Zn(OH)_4^{2-}$ deposition/dissolution on the 3D porous carbon felt in the alkaline electrolyte.

Although excellent battery performance and cycling stability have been achieved, the concentration of active species in the supporting electrolyte is limited, leading to a low energy density. Thus to verify the practicability and afford a high-energy-density alkaline zinc-iron flow battery, further work was carried out to increase the active species concentration in both positive and negative electrolytes, which is highly desirable for practical application of a flow battery. Normally, $K_4Fe(CN)_6$ [or $Na_4Fe(CN)_6$] has a low solubility in KOH (or NaOH) solutions because of the "common ion effect." Therefore to avoid the common ion effect, we opt to use sodium ferrocyanide as the positive active material, which affords a concentration of 1 mol L^{-1} in 3 mol L^{-1} potassium hydroxide supporting electrolyte (Xia et al., 2012), and 0.5 mol L^{-1}

$Zn(OH)_4^{2-}$ dissolved in 4 mol L^{-1} sodium hydroxide as the negative electrolyte. The resulting flow battery with a self-made membrane demonstrated a well-defined OCV of 1.83 V at 50% states of charge (SOC). The OCV was monotonically increased from 1.74 to 1.96 V with SOC increasing from 5% to 90%, as evidenced in Figure S8. This OCV was higher than the estimated thermodynamic potential of 1.63 V, which was mainly attributed to the formation of cationic complexes with $Fe(CN)_6^{3-}$ and $Fe(CN)_6^{4-}$ ions (McBreen, 1984). The flow battery with a self-made membrane exhibited a discharge capacity and energy of ~24 Ah L^{-1} and ~40 Wh L^{-1}, respectively, achieving an electrolyte utilization of ~90% (theoretical capacity of 26.76 Ah L^{-1}) at a current density of 60 mA cm^{-2} (Figure S9A). The CE, EE, and VE are 99.15%, 91.28%, and 92.06%, respectively, exhibiting a stable cycling performance for about 150 cycles (Figures S9B–S9D). By operating at a current density of 80 mA cm^{-2}, a CE of 99.71%, an EE of 89.59%, and an electrolyte utilization of ~80% can be achieved, as shown in Figure S10A, demonstrating a stable battery performance (Figures S10B and S10C) and a super-high-capacity retention (Figure S10D) for more than 200 cycles.

This excellent battery performance clearly validates the practicability of the alkaline zinc-iron flow battery. Nevertheless, the current density is relatively low, which may indeed affect the output power density of a battery. Therefore we further tested the alkaline zinc-iron flow battery by varying the current density from 60 to 160 mA cm^{-2}. As expected, the battery still can deliver an outstanding battery performance, maintaining a CE of nearly 100% (Figures 2A and B). For instance, the battery exhibited no decrease in CE (~100%) and EE (~86%) after more than 200 cycles at a current density of 100 mA cm^{-2} (Figures 2A and 2C). It was also observed that this battery could be charged and discharged for about 40 min for each cycle while preserving a steady discharge capacity of above 21 Ah L^{-1} and discharge energy of above 34 Wh L^{-1} as the cycle proceeded (Figure 2C). Even at the high current density of 160 mA cm^{-2}, the battery demonstrates an average VE of 83.20% and an average EE of 82.78% (Figure 2D), maintaining this performance over more than 150 cycles, together with a stable discharge capacity of 15.92 Ah L^{-1} and a discharge energy of 25.43 Wh L^{-1} (Figure 2D). Owing to the high CE of the battery, the discharge capacity of the battery remained nearly unchanged, yielding a capacity retention of over 99.999% per cycle. Such high performance at such high working current density is first reported among the newly developed flow battery systems. The battery shows comparable performance to a vanadium flow battery, although with a much lower cost and much higher power density owing to its higher OCV, showing promising prospect in large-scale energy storage.

The Role of Membrane

To better understand the role of a PBI membrane, the performance of a battery assembled with a cation-conducting membrane (Nafion 115 membrane) was used for comparison. The surface and cross section of PBI (Figure S11) and Nafion 115 (Figure S12) membranes both demonstrated a smooth and dense structure. The distribution of negatively charged sulfonated groups of Nafion 115 can be further confirmed by transmission electron microscopy (Figure S12D). A battery assembled with a Nafion 115 membrane delivered a CE of 99.20%, an EE of 78.83%, and a VE of 79.46% at a current density of 80 mA cm^{-2} (Figure S13A), which is much lower than that delivered by a battery with a self-made PBI membrane. A battery with a Nafion 115 membrane shows a much higher initial charge-discharge voltage gap (145.1 mV) than a battery with a self-made membrane (49.78 mV) (Figure S13B), indicating a much higher ohmic polarization for the battery with a Nafion 115 membrane. The impedance Nyquist plot of a battery with a Nafion 115 membrane at 50% SOC demonstrates an ohmic resistance of 2.144 Ω cm^2, which is nearly 2-fold higher than that of a battery with a self-made PBI membrane (1.152 Ω cm^2) (Figure S14), further confirming the above-mentioned results. We propose that the poor performance of Nafion 115 membrane in this system originates from the repulsion effect between the negatively charged sulfonated groups in Nafion 115 (Figure S12D) and the negatively charged hydroxyl ions in the electrolyte, leading to poor ion conductivity. On the other hand, Nafion 115 has a more continuous phase-separated structure (Figures S15A and S15B) than a PBI membrane (Figures S15C and S15D). The hydrophilic phase from sulfonated acid groups of Nafion 115 results in a membrane with a swelling of 11.11%, which is much higher than that of a PBI membrane (4.348%). The continuous phase-separated structure together with high swelling of Nafion 115 may possibly result in zinc growth into the membrane easily during the charging process (Figure S16), further leading to high resistance of the membrane. By contrast, the PBI membrane is a totally aromatic rigid polymer and has very low swelling in aqueous solution, showing no obvious phase separation structure (Figures S15C and S15D); however, it can still easily transfer OH^- by Grotthuss mechanism from imidazolyl groups. Taking the above-mentioned advantages into consideration, no obvious zinc dendrite and zinc accumulation, which are regarded as the two major issues hindering the commercial application of zinc-based batteries,

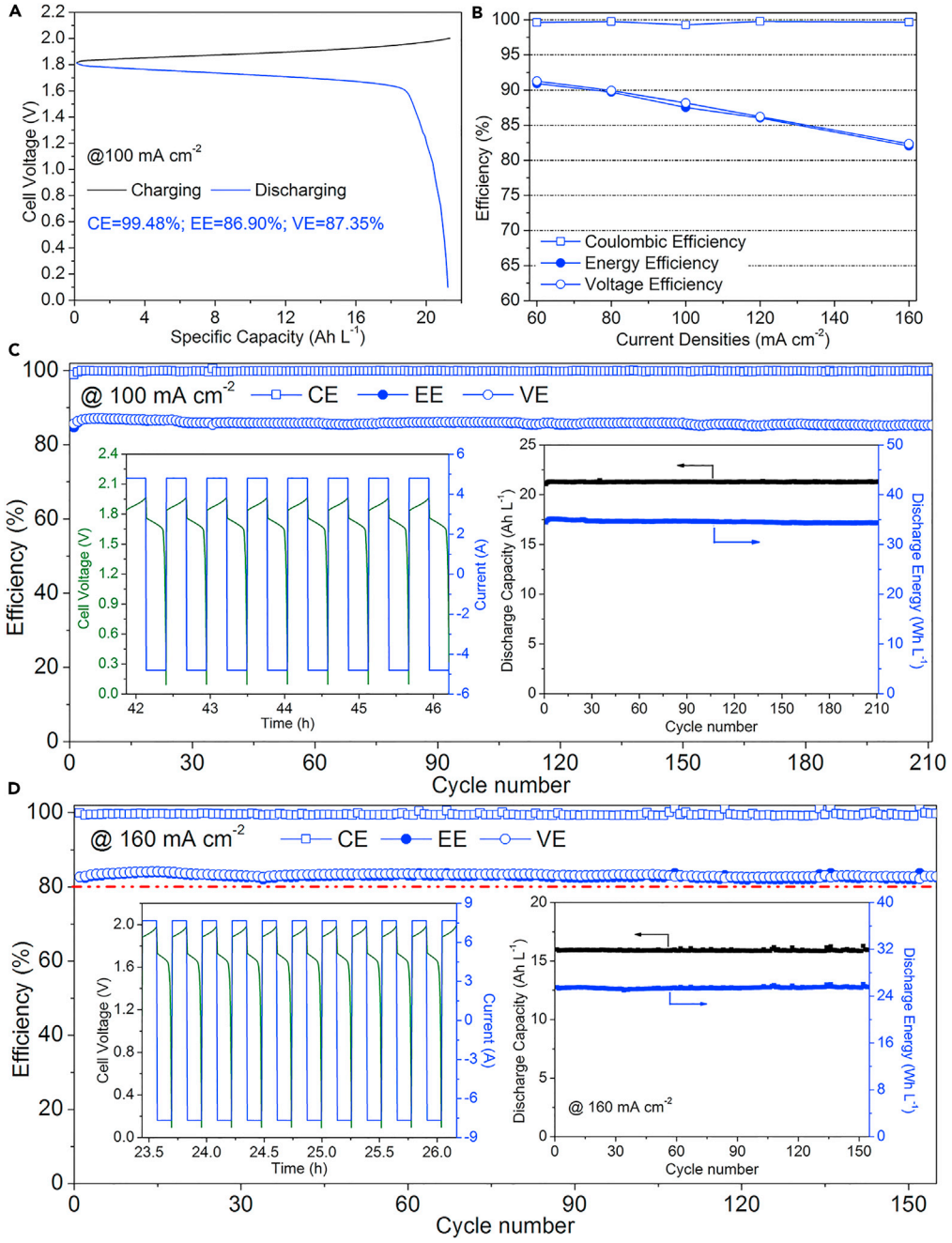

Figure 2. Performance of the Alkaline Zinc-Iron Flow Battery Using a High-Concentration Electrolyte

(A) Cell voltage profiles of the alkaline zinc-iron flow battery with self-made PBI membrane at a current density of 100 mA cm^{-2}.

(B) The performance of an alkaline zinc-iron flow battery with self-made membrane with current densities ranging from 60 mA cm^{-2} to 160 mA cm^{-2}.

(C) The cycling performance of an alkaline zinc-iron flow battery at 100 mA cm^{-2}. Insert, representative charge and discharge curves of the alkaline zinc-iron flow battery and the corresponding discharge capacity and discharge energy for each cycle.

(D) The cycling performance of an alkaline zinc-iron flow battery at 160 mA cm^{-2}. Insert, representative charge and discharge profiles of the alkaline zinc-iron flow battery and the corresponding discharge capacity and discharge energy for each cycle. 60 mL 1.0 mol L^{-1} $Na_4Fe(CN)_6$ + 3 mol L^{-1} potassium hydroxide solution and 60 mL 0.5 mol L^{-1} $Zn(OH)_4^{2-}$ + 4 mol L^{-1} sodium hydroxide solution were used as the positive and negative electrolytes, respectively.

See also Figures S1, S5–S10, S13, S14, S17, and S21.

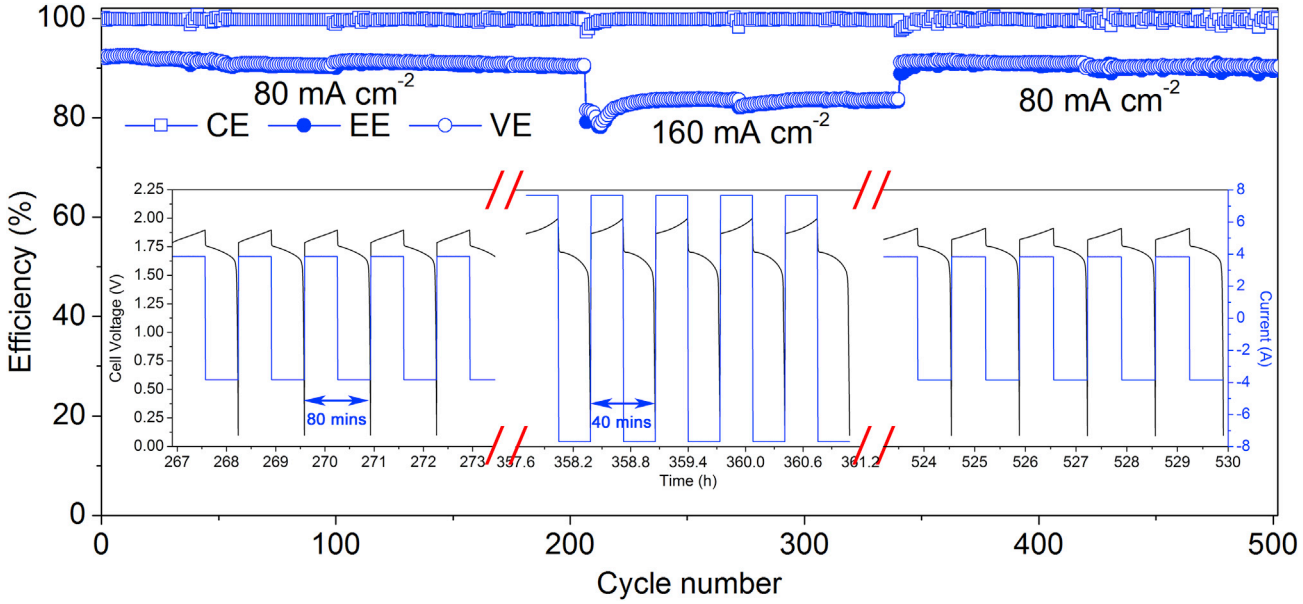

Figure 3. Long-Term Stability of the Self-made Polybenzimidazole Membrane

180 mL 1.0 mol L-1 $Na_4Fe(CN)_6$ + 3 mol L^{-1} potassium hydroxide solution and 180 mL 0.5 mol L^{-1} $Zn(OH)_4^{2-}$ + 4 mol L^{-1} sodium hydroxide solution were used as the positive and negative electrolytes, respectively. The charging process was controlled by the charging time (40 min for 80 mA cm^{-2} and 20 min for 160 mA cm^{-2}) to maintain the constant charge capacity, and the discharge process was ended with the cutoff voltage of 0.1 V. Thus the duration of each cycle was 80 min at 80 mA cm^{-2} and 40 min at 160 mA cm^{-2}, respectively.

See also Figures S1, S7, S8, S14, and S19.

could be observed on the carbon felt electrode by using a PBI membrane after charge and discharge cycling test, as shown in Figure S17. By contrast, the metallic zinc deposited on the electrode was found to be dense (Figures S18A–S18C) and obvious metallic zinc accumulation can be observed (Figures S18A′–S18C′) after cycling test by employing a Nafion 115 membrane. Taking the fast transportation of OH^- through Grotthuss mechanism, no obvious phase separation structure, and the high mechanical stability of PBI together, a battery with a PBI membrane could retain a lower membrane resistance and higher VE than a Nafion 115 membrane, and the zinc dendrite and accumulation can be effectively prevented by artistically introjecting this membrane with our flow battery configuration.

The chemical stability of membrane materials during the charging-discharging process is one of the most critical concerns that affects the cycling stability of a flow battery system. Figure 3 shows the cycling stability of an alkaline zinc-iron flow battery using a self-made PBI membrane after treating it in 3 mol L^{-1} sodium hydroxide solution at 30°C for more than 1 month. The battery with the alkaline-treated membrane showed stable performance after continuously running for more than 500 cycles over a range of current densities (80–160 mA cm^{-2}), suggesting that this kind of membrane can withstand the alkaline electrolyte solution in the long term (the battery runs 370 cycles at 80 mA cm^{-2} and 135 cycles at 160 mA cm^{-2}. The duration of each cycle was 80 min for 80 mA cm^{-2} and 40 min for 160 mA cm^{-2}. Thus the total time consumed for this test was 583 hr, which is long enough among the recently reported new flow battery systems). The surface and cross-sectional morphologies of the self-made PBI membrane after the flow battery cycling experiment were detected by field emission scanning electron microscope (FE-SEM) to further verify the membrane stability. As displayed in Figures S19A and S19B, similar to the pristine membrane (Figures S11A and S11B), a smooth and dense structure can be clearly observed, indicating that the membrane possesses excellent stability under alkaline medium. Besides, the membrane surface toward the positive half-cell remained flat and dense as well (Figure S19D), whereas the membrane surface facing the negative half-cell showed a relatively rough but still an integral morphology (Figure S19C), which was mainly attributed to the uneven plating/stripping of zinc during the charging and discharging process at high current density (160 mA cm^{-2}). On the other hand, although $[Fe(CN)_6]^{3-/4-}$ was reported to experience degradation in strong alkaline solution to some extent (Soloveichik, 2015; McBreen, 1984; Luo et al., 2017a), our long-term cycle experiment demonstrates that the degradation

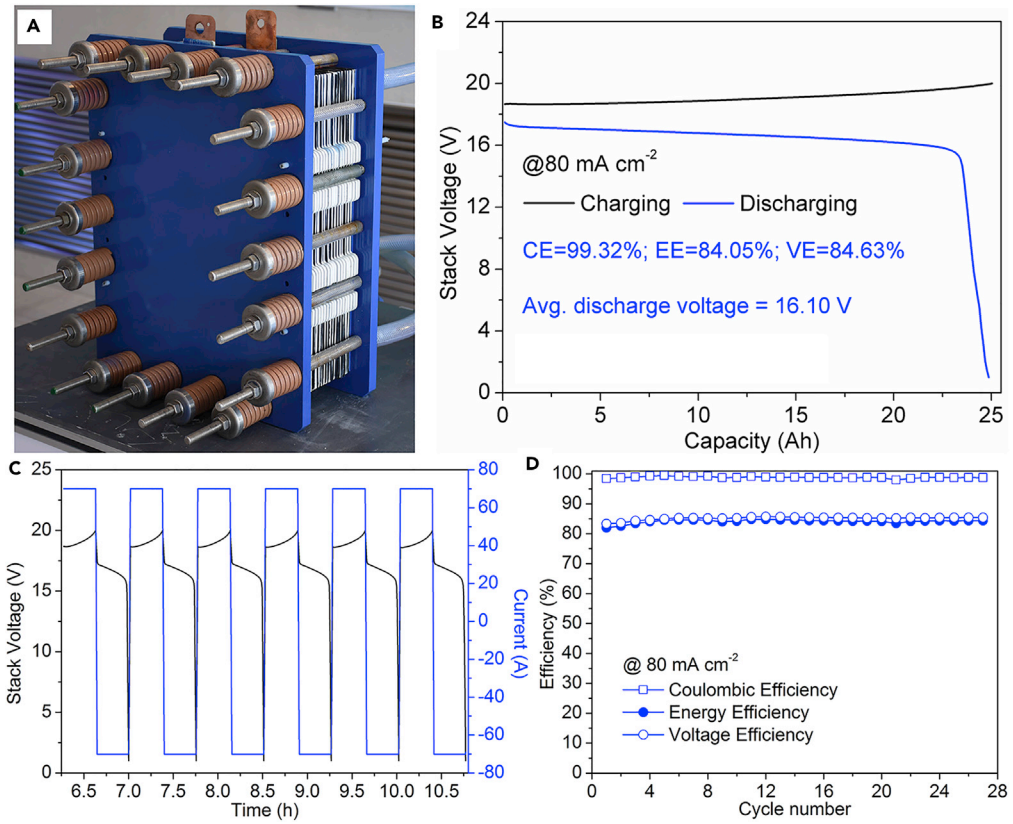

Figure 4. Practical Realization of the Alkaline Zinc-Iron Flow Battery

(A) The kW alkaline zinc-iron flow battery cell stack prototype using self-made, low-cost non-fluorinated ion-exchange membrane.

(B) Cell stack voltage profile of the alkaline zinc-iron flow battery at a current density of 80 mA cm^{-2}.

(C) Parts of charge and discharge curves of the cell stack.

(D) Cycle performance of the cell stack at a current density of 80 mA cm^{-2}.

See also Figures S1 and S11.

of $[Fe(CN)_6]^{3-/4-}$ in our system is negligible and has little effect on the battery performance. Overall, the PBI membrane demonstrated an excellent stability in this alkaline zinc-iron flow battery medium.

The Role of 3D Porous Carbon Felt Electrode

To investigate the role of a 3D porous carbon felt electrode, a battery with a PBI membrane using a zinc plate as the negative electrode (Figure S20A) was assembled. Shown in Figure S20 is the battery performance using a zinc plate electrode, affording a CE of 99.39% and an EE of 78.52% at a current density of 80 mA cm^{-2} (Figure S20B), which is much lower than that of a battery employing a 3D porous carbon felt as the electrode at the same condition. In addition, an uneven zinc plating (Figures S20C and S20E) and a distinctly severe zinc accumulation (Figures S20D and S20F) can be found for the battery using a zinc plate as the electrode at the end of charging and discharging. Even at a high CE of 99.39%, zinc accumulation still remained due to the poor connectivity between the deposited metallic zinc and the zinc plate electrode, further resulting in poor electronic conduction of the deposited metallic zinc. As a consequence, the $Zn(OH)_4^{2-}$ ions in the electrolyte were plated perpetually during charging, whereas metallic zinc on the zinc plate electrode was stripped during discharging, which eventually led to the zinc electrode being deformed and eroded. However, for a battery employing a 3D porous carbon felt with high specific surface area as the electrode, the zinc deposition (Figures S17A–S17C) and accumulation (Figures S17A′–S17C′) were significantly improved. Even with current densities increasing from 60 mA cm^{-2} to 160 mA cm^{-2}, no significant difference in the morphologies of zinc deposited on the 3D porous carbon felt electrode could be observed, as shown by the results of scanning electron microscopy (Figure S21). This highly porous carbon felt considerably reduces the

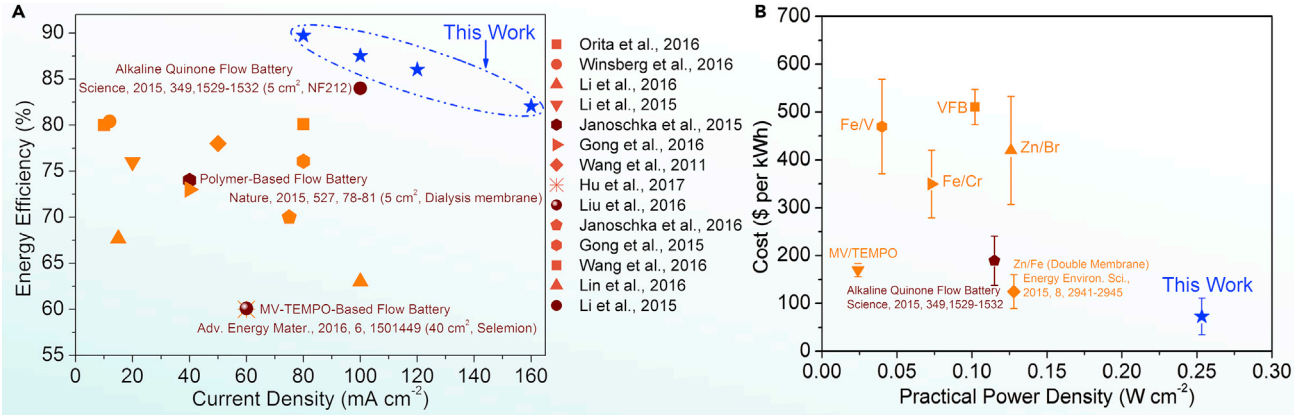

Figure 5. Comparison of Both Recently Reported Flow Battery Systems and Traditional Flow Battery Systems with the Alkaline Zinc-Iron Flow Battery

(A) The performance of recently reported flow batteries. Most of these flow batteries use Nafion series membranes, which result in the high cost of the system.

(B) The cost and practical output power densities for different flow battery systems and the alkaline zinc-iron flow battery system. The practical output power densities were calculated from the charge-discharge curves of the single cells (the peak power density obtained from a polarization curve of a given flow battery was not considered here since at the point of the peak power density, the current density is normally much higher, e.g., higher than 600 mA cm^{-2}; under this condition, the battery efficiency is too low, or the battery is difficult to work anymore). The error bars are defined as the cost fluctuations under different current density.

See also Figure S12 and Tables S1–S6.

internal resistance of the interface between the electrode and deposited metallic zinc and prevents metallic zinc from falling (Figures S17A and S17B) before reaction because of the 3D porous structure. The high specific surface is propitious to further reduce polarization and improve the zinc deposition efficiency. During the charging process, the $Zn(OH)_4^{2-}$ was reduced and deposited on the porous carbon felt electrode, forming porous carbon felt/metallic zinc composite electrode (Figures S17B and S17C). Similar to previous reports (Luo et al., 2017b; Zhang et al., 2017), the pores of carbon felt could serve as a guidance on which the zinc stripping/plating processes can take place and effectively suppress the zinc dendrite/accumulation that occurs. During this process, OH^- was released and transferred through the membrane to complete the internal circuit. The OH^- in the negative electrolyte can go through the deposited metallic zinc and arrive at the positive half-cell in due time. Therefore the $Zn(OH)_4^{2-}$ in the bulk solution can be reduced and deposited on both the inner porous carbon felt and metallic zinc electrode. On the contrary, in the discharging process the metallic zinc was oxidized to $Zn(OH)_4^{2-}$ and OH^- was consumed, which results in a concentration gradient between the positive and negative regions. Thus the fast transportation of OH^- through the membrane can realize the fast oxidization of Zn on the porous carbon felt electrode, improving the accumulation of metallic zinc on the electrode. In addition, the deposition of metallic zinc on the porous carbon felt electrode was porous (Figure S14C). The porous metallic zinc can allow OH^- to diffuse into the inner metallic zinc and electrode, which makes the metallic zinc deposited on the inner carbon felt discharged completely, as shown in Figure S17C′.

Practicability of the Alkaline Zinc-Iron Flow Battery System

Finally, to further confirm the practicability of the alkaline zinc-iron flow battery system, a kilowatt cell stack (Figure 4A) was assembled by using the self-made PBI membrane. Figures 4B–4D displayed the cell stack performance. The cell stack itself demonstrates an average CE of 98.84%, an average EE of 84.17%, and a VE of 85.16% at a current density of 80 mA cm^{-2}, affording an average output power of 1.127 kW and an average discharge voltage of 16.10 V. Taking the advantages of the low-cost redox couples, self-made membrane, bipolar plate, and high voltage, a capital cost under $90 per kW h can be obtained (Tables S1–S6), which is much lower than the Department of Energy's cost target ($150 per kW h). To the best of our knowledge, this is the first time that a kW cell stack with a self-made, inexpensive membrane and such a low capital cost has been assembled and reported among the newly developed flow battery systems. Taken together, the excellent battery and cell stack performance (efficiencies and output power density) (Figures 5A and 5B), high energy density, and the super-low cost (Figure 5B) make the alkaline zinc-iron flow battery very promising for stationary energy storage.

Conclusion

In summary, we have demonstrated an ultra-high performance alkaline zinc-iron flow battery that can be operated at a wide range of current densities (60–160 mA cm^{-2}). The battery exhibited very high power density, energy density, and efficiencies. Most importantly, by using the self-made, low-cost PBI membrane with ultra-high chemical stability, 3D porous carbon felt electrode, and inexpensive zinc and iron active materials, the cost of zinc/iron battery system is even lower than $90/kWh. The results indicated that the alkaline zinc-iron flow battery system is one of the most promising candidates for next-generation large-scale energy storage systems.

METHODS

All methods can be found in the accompanying Transparent Methods supplemental file.

SUPPLEMENTAL INFORMATION

Supplemental Information includes Transparent Methods, 21 figures, and 6 tables and can be found with this article online at https://doi.org/10.1016/j.isci.2018.04.006.

ACKNOWLEDGMENTS

The authors greatly acknowledge the financial support from China Natural Science Foundation (Grant Nos. 21206158), Key project of Frontier Science, CAS (QYZDB-SSW-JSC032), CAS-DOE collaborative project, DICP&QIBEBT funding (DICP&QIBEBT UN201707) and DICP funding (ZZBS201707).

AUTHOR CONTRIBUTIONS

Z.Y. performed the experiments, analyzed the data, and wrote the initial manuscript draft. Y.D. performed the experiments and analyzed the data. Z.Y. and Y.D. contributed equally to this work and should be considered co-first authors. Prof. X.L. designed and oversaw the experiments and revised and finalized the manuscript for submission. Prof. H.Z. and T.L. participated in the discussions of the results. All authors reviewed the manuscript.

DECLARATION OF INTERESTS

The authors declare no financial interest and have a patent related to this work.

Received: December 19, 2017
Revised: March 7, 2018
Accepted: March 22, 2018
Published: May 25, 2018

REFERENCES

Adams, G.B. (1979). Electrically Rechargeable Battery (Google Patents).

Adams, G., Hollandsworth, R., and Webber, B. (1979). Rechargeable Alkaline Zinc/Ferricyanide Battery (Lockheed Missiles and Space Co), Report, 1.

Cheng, Y., Zhang, H.M., Lai, Q., Li, X., Shi, D., and Zhang, L. (2013). A high power density single flow zinc–nickel battery with three-dimensional porous negative electrode. J. Power Sources *241*, 196–202.

Chu, S., Cui, Y., and Liu, N. (2017). The path towards sustainable energy. Nat. Mater. *16*, 16–22.

Dunn, B., Kamath, H., and Tarascon, J.M. (2011). Electrical energy storage for the grid: a battery of choices. Science *334*, 928–935.

Gong, K., Ma, X., Conforti, K.M., Kuttler, K.J., Grunewald, J.B., Yeager, K.L., Bazant, M.Z., Gu, S., and Yan, Y. (2015). A zinc–iron redox-flow battery under $100 per kW h of system capital cost. Energy Environ. Sci. *8*, 2941–2945.

Gong, K., Xu, F., Grunewald, J.B., Ma, X., Zhao, Y., Gu, S., and Yan, Y. (2016). All-soluble all-iron aqueous redox-flow battery. ACS Energy Lett. *1*, 89–93.

Hu, B., Debruler, C., Rhodes, Z., and Liu, T. (2017). A long cycling aqueous organic redox flow battery (AORFB) towards sustainable and safe energy storage. J. Am. Chem. Soc. *139*, 1207–1214.

Janoschka, T., Martin, N., Martin, U., Friebe, C., Morgenstern, S., Hiller, H., Hager, M.D., and Schubert, U.S. (2015). An aqueous, polymer-based redox-flow battery using non-corrosive, safe, and low-cost materials. Nature *527*, 78–81.

Janoschka, T., Martin, N., Hager, M.D., and Schubert, U.S. (2016). An Aqueous redox-flow battery with high capacity and power: the TEMPTMA/MV system. Angew. Chem. Int. Ed. *55*, 14427–14430.

Li, Q., He, R., Jensen, J.O., and Bjerrum, N.J. (2003). Approaches and recent development of polymer electrolyte membranes for fuel cells operating above 100°C. Chem. Mater. *15*, 4896–4915.

Li, B., Nie, Z., Vijayakumar, M., Li, G., Liu, J., Sprenkle, V., and Wang, W. (2015). Ambipolar zinc-polyiodide electrolyte for a high-energy density aqueous redox flow battery. Nat. Commun. *6*, 6303.

Li, Z., Weng, G., Zou, Q., Cong, G., and Lu, Y.C. (2016). A high-energy and low-cost polysulfide/iodide redox flow battery. Nano Energy *30*, 283–292.

Lin, K., Chen, Q., Gerhardt, M.R., Tong, L., Kim, S.B., Eisenach, L., Valle, A.W., Hardee, D., Gordon, R.G., Aziz, M.J., et al. (2015). Alkaline quinone flow battery. Science *349*, 1529–1532.

Lin, K., Gómez-Bombarelli, R., Beh, E.S., Tong, L., Chen, Q., Valle, A., Aspuru-Guzik, A., Aziz, M.J., and Gordon, R.G. (2016). A redox-flow battery with an alloxazine-based organic electrolyte. Nat. Energy *1*, 16102.

Liu, T., Wei, X., Nie, Z., Sprenkle, V., and Wang, W. (2016). A total organic aqueous redox flow battery employing a low cost and sustainable methyl viologen anolyte and 4-HO-TEMPO catholyte. Adv. Energy Mater. *6*, 1501449.

Luo, J., Sam, A., Hu, B., DeBruler, C., Wei, X., Wang, W., and Liu, T.L. (2017a). Unraveling pH dependent cycling stability of ferricyanide/ferrocyanide in redox flow batteries. Nano Energy *42*, 215–221.

Luo, W., Zhang, Y., Xu, S., Dai, J., Hitz, E., Li, Y., Yang, C., Chen, C., Liu, B., and Hu, L. (2017b). Encapsulation of metallic Na in an electrically conductive host with porous channels as a highly stable Na metal anode. Nano Lett. *17*, 3792–3797.

McBreen, J. (1984). Rechargeable zinc batteries. J. Electroanal. Chem. Interfacial Electrochem. *168*, 415–432.

Orita, A., Verde, M.G., Sakai, M., and Meng, Y.S. (2016). A biomimetic redox flow battery based on flavin mononucleotide. Nat. Commun. *7*, 13230.

Park, M., Ryu, J., Wang, W., and Cho, J. (2016). Material design and engineering of next-generation flow-battery technologies. Nat. Rev. Mater. *2*, 16080.

Perry, M.L., and Weber, A.Z. (2015). Advanced redox-flow batteries: a perspective. J. Electrochem. Soc. *163*, A5064–A5067.

Selverston, S., Savinell, R.F., and Wainright, J.S. (2016). In-tank hydrogen-ferric ion recombination. J. Power Sources *324*, 674–678.

Selverston, S., Savinell, R.F., and Wainright, J.S. (2017). Zinc-iron flow batteries with common electrolyte. J. Electrochem. Soc. *164*, A1069–A1075.

Soloveichik, G.L. (2015). Flow batteries: current status and trends. Chem. Rev. *115*, 11533–11558.

Wang, W., Kim, S., Chen, B., Nie, Z., Zhang, J., Xia, G., Li, L., and Yang, Z. (2011). A new redox flow battery using Fe/V redox couples in chloride supporting electrolyte. Energy Environ. Sci. *4*, 4068–4073.

Wang, C., Li, X., Xi, X., Zhou, W., Lai, Q., and Zhang, H.M. (2016). Bimodal highly ordered mesostructure carbon with high activity for Br2/Br− redox couple in bromine based batteries. Nano Energy *21*, 217–227.

Winsberg, J., Janoschka, T., Morgenstern, S., Hagemann, T., Muench, S., Hauffman, G., Gohy, J.F., Hager, M.D., and Schubert, U.S. (2016). Poly(TEMPO)/zinc hybrid-flow battery: a novel, "green," high voltage, and safe energy storage system. Adv. Mater. *28*, 2238–2243.

Xia, G., Yang, Z., Li, L., Kim, S., Liu, J., and Graff, G.L.. (2012). Iron-Sulfide Redox Flow Batteries. United States Patent Application Publication, Pub. NO.: US 2012/0244406 A0244401

Yang, Z., Zhang, J., Kintner-Meyer, M.C., Lu, X., Choi, D., Lemmon, J.P., and Liu, J. (2011). Electrochemical energy storage for green grid. Chem. Rev. *111*, 3577–3613.

Yuan, Z., Duan, Y., Zhang, H., Li, X., Zhang, H.M., and Vankelecom, I. (2016a). Advanced porous membranes with ultra-high selectivity and stability for vanadium flow batteries. Energy Environ. Sci. *9*, 441–447.

Yuan, Z., Zhu, X., Li, M., Lu, W., Li, X., and Zhang, H.M. (2016b). A highly ion-selective zeolite flake layer on porous membranes for flow battery applications. Angew. Chem. Int. Ed. *55*, 3058–3062.

Zhang, Y., Luo, W., Wang, C., Li, Y., Chen, C., Song, J., Dai, J., Hitz, E.M., Xu, S., Yang, C., et al. (2017). High-capacity, low-tortuosity, and channel-guided lithium metal anode. Proc. Natl. Acad. Sci. USA *114*, 3584–3589.

ISCI, Volume *3*

Supplemental Information

Toward a Low-Cost Alkaline Zinc-Iron Flow Battery with a Polybenzimidazole Custom Membrane for Stationary Energy Storage

Zhizhang Yuan, Yinqi Duan, Tao Liu, Huamin Zhang, and Xianfeng Li

Supplemental Information

Transparent Methods

Materials

Potassium hexacyanoferrate, potassium ferrocyanide, potassium hydroxide, N,N-dimethylacetamide (DMAc) were purchased from Tianjin Damao Chemical Reagent Factory. Sodium hydroxide was purchased from Tianli Chemical Reagent Co.,Ltd. Sodium ferrocyanide was bought from Sinopharm Chemical Regent Co.,Ltd. Zinc oxide was bought from Kermel Chemical Reagent Factory. These reagents were supplied with analytical grade. Other reagents were brought from Sigma Aldrich unless stated otherwise and used as received.

Polybenzimidazole (PBI) Polymer Synthesis and Characterization

The PBI was synthesized by condensation polymerization of 3,3'-diaminobenzidine (DABz, Acros Organic) and 4,4'-dicarboxydiphenylether (DCDPE, Peak-chem, Shanghai, China) at 140 ℃ in phosphorus pentoxide/methanesulfonic acid.(Dai et al., 2010, Chen et al., 2015) After decontamination, PBI was obtained as a yellow powder. The dynamic viscosity of the synthesized PBI polymer, determined by a NDJ-8S viscometer (Shanghai Pingxuan scientific instrument Co., Ltd, China) at 25 ± 1 ℃ with a concentration of 17 wt.% in DMAc, was 304.8 Pa·s. To detect the chemical structure of the PBI polymer, Fourier transformed infrared spectroscopy (BRUKER TENSOR 27), recorded at an average rate of 48 scans with a resolution of 4 cm^{-1} and collected from 600 to 4000 cm^{-1} in reflection model, was employed. Nuclear magnetic resonance (^{1}H NMR), recorded on BRUKER DRX400 by using DMSO-d6 as solvent and tetramethylsilane (TMS) as internal standard, was used to further confirm the

chemical structure of prepared PBI.

Self-made, Low Cost PBI Membrane Preparation

The self-made, low cost PBI membrane was prepared by dissolving the PBI polymer in DMAc to form a 17 wt.% solution. The solution was cast onto a clean glass plate using a doctor blade (Elcometer 3545 adjustable Bird Coater, Scraper, Elcometer 3545/8) and then dried at 50 ℃ for 24 hours. Afterwards, the membrane was peeled off from the glass plate. The thickness of the membrane was approximately 35 μm. The prepared membrane was soaked in 3 mol L^{-1} sodium hydroxide solution for 5 hours before battery or stack performance measurement.

Mechanical Properties of PBI and Nafion 115 membranes

The mechanical properties of the self-made PBI and Nafion 115 membranes were determined by a material test-machine (AG-2004, Shimadzu) at a loading velocity of 5 cm min^{-1}. Each result was an average value of at least three parallel experiments.

Permeability of Anionic Active Species through the PBI membrane

The permeability of anionic active species through the PBI membrane was determined by a diffusion cell separated by a membrane. The left cell was filled with 0.4 mol L^{-1} anionic active species ($K_4Fe(CN)_6$, $K_3Fe(CN)_6$ or $Na_2Zn(OH)_4$) in 3 mol L^{-1} sodium hydroxide solution (volume: 80 mL) while the right one was filled with 0.4 mol L^{-1} K_2SO_4 in a 3 mol L^{-1} sodium hydroxide solution (volume: 80 mL) to equalize the ionic strengths and minimize the osmotic pressure effects. Solutions in both half cells were vigorously stirred to avoid concentration polarization. The effective area of the membrane was 9 cm^2. Samples of a 3 mL solution from the right cell were collected at

a regular time interval. Another 3 mL fresh K_2SO_4 solution was then added to the right cell to keep the solution volume stable. The $K_4Fe(CN)_6$ or $K_3Fe(CN)_6$ concentration of the samples was detected using a UV-vis spectrometer. The $Na_2Zn(OH)_4$ concentration of the samples was detected using a inductively coupled plasma mass spectrometry (ICP-MS). The anionic active species permeability was calculated according to Fick's diffusion law as the following equation:

$$V_B \frac{dC_B(t)}{dt} = A\frac{p}{L}(C_A - C_B(t))$$

where V_B is the solution volume in the right reservoir, $C_B(t)$ is anionic active species concentration in the left cell as a function of time t, while A and L are the effective area and thickness of the membrane, respectively. P is the permeability of anionic active species, and C_A is the anionic active species concentration in the left cell.

Membrane Morphology

The morphologies of the PBI and Nafion 115 membranes surface and cross section were recorded by scanning electron microscope (JSM-7800F) equipped with energy dispersive X-ray spectroscope (EDS). The cross section of the membrane was obtained by breaking the membranes in liquid nitrogen and coating them with gold prior to imaging. Both membrane surface and cross section were demonstrated a flat and dense morphology. The EDS spectrum of the membrane surface confirmed that the prepared PBI membrane was composed of the elements carbon, nitrogen and oxygen. The morphology of the hydrophilic domains of Nafion 115 membrane was recorded by using TEM (JEM-2000EX, JEOL). Nafion 115 membrane was first converted to the Pb^{2+} form by immersing in lead acetate solution (0.5 M) for 3 days

and then fixed in epoxy, before cutting it into thin slice. The sample was cast onto a Cu grid for TEM study.

Membrane Swelling

The swelling of the PBI and Nafion 115 membranes was measured as follows: the PBI and Nafion 115 membranes with fixed length were first soaked in deionized water for 3 days in order to saturate them with water. The length of the saturated membranes was then obtained. The swelling is defined as the length ratio of the swollen membranes to the dry membranes, as shown in the following equation:

$$Swelling\ (\%) = \frac{L_s - L_d}{L_d} \times 100$$

Where L_s and L_d are the length of saturated and dry membrane, respectively.

Electrochemical Characterization

Cyclic voltammetry (CV) was performed on a Gamry Multichannel System installation (Reference 3000) employing a three-electrode cell with a graphite plate working electrode (1 cm^2), a Hg/HgO reference electrode and a graphite plate counter electrode. The CV tests were conducted at different sweeping rates at room temperature. EIS was performed at 50% SOC with frequency ranging from 100000 Hz to 0.1 Hz. The RDE experiment was measured from -1.4 V to -1.8 V versus Hg/HgO at a sweep rate of 10 mVs^{-1}, during which time the electrode was rotated at 100 RPM to 600 RPM. The limiting currents were plotted versus the rotation rate. The slope was fit using the Levich equation. The transfer coefficient was calculated using the Koutecky′–Levich equation.

Battery Performance

The alkaline zinc-iron flow battery was assembled by sandwiching a self-made membrane between two carbon felt electrodes (porosity and surface area of the carbon felt are 94% and 7.5 m^2/g), clamped by two graphite plates. The active area of the electrode is 6×8 cm^2. All of these components were fixed between two stainless steel plates. The electrolyte was cyclically pumped through the corresponding electrodes in airtight pipelines. Charge-discharge cycling tests were conducted by ArbinBT 2000 at a constant current density ranging from 60 to 160 mA cm^{-2}. The charge process was controlled by the charge time to keep a constant charge capacity, while the discharge process was ended with the cut-off voltage of 0.1 V. The state-of-charge (SOC) vs. open circuit voltage (OCV) data was measured by incremented charging time (150 s) at 40 mA cm^{-2}.

The Stability Test of the Prepared Membrane

To investigate the stability of the prepared membrane, PBI membrane was soaked in 3 mol L^{-1} sodium hydroxide solution at 30 ℃ for more than 31 days. Afterwards, the alkaline zinc-iron single cell test operating at a constant current density ranging from 80 to 160 mA cm^{-2}, was performed on the treated membrane. After the cycling performance test, the morphology of the membrane was detected by SEM to further investigate the stability of the PBI membrane under the alkaline medium.

The Alkaline Zinc-Iron Flow Battery Stacks

A kilowatt level cell stack was assembled to confirm the reliability and practicality of the alkaline zinc-iron flow battery by employing the self-made membrane. The stack was constructed by pressing 10 alkaline zinc-iron single cells together. The effective

electrode area was 875 cm^2. For each single cell, it was prepared with two carbon felt electrodes at each side of the self-made membrane as positive and negative electrode, respectively, self-made carbon plastic bipolar plates, PVC frames and gaskets. The alkaline zinc-iron flow battery system was assembled by connecting the stack with the negative and positive electrolyte tanks by two pumps and pipes as described elsewhere. Solutions consisting of 20 L 1.0 mol L^{-1} $Na_4Fe(CN)_6$ + 3 mol L^{-1} potassium hydroxide solution and 20 L 0.5 mol L^{-1} $Zn(OH)_4^{2-}$ + 4 mol L^{-1} sodium hydroxide solution were used as positive and negative electrolytes, respectively. The $Zn(OH)_4^{2-}$ was prepared by dissolving ZnO in sodium hydroxide solution.

Cost Calculations

For a flow battery widely utilized in energy storage, the cost is one of the most important prerequisites.(Viswanathan et al., 2014, Shah et al., 2011) Thus the capital cost of the alkaline zinc-iron flow battery, which mainly includes the cost of electrolyte and stack, was calculated by the following equation.(Gong et al., 2015) Note our calculating is based on a two hours system since the areal capacity is limited for zinc based flow battery.

$$C_{sys} \approx C_e + C_s = U_e/V_{eff} + U_s/(t \cdot I \cdot V_{eff})$$

where C_{sys}, C_e and C_s are cost of system, electrolyte and stack ($ per kWh), respectively; Us is the unit stack price which contains electrodes, membranes and bipolar plates ($ per m^2); V_{eff} is the effective discharge cell voltage (V); t is the designed discharge duration (h); and I is the current density (A m^{-2}).

The electrolyte cost was calculated according to the following equation and the results

are listed in Table S1.

$$U_e=U_r+U_{se}=(u_{r,n}+u_{r,p})+(u_{se,n}+u_{se,p})$$

Where U_e is the electrolyte cost, U_r is the cost of the redox couple; U_{se} is the cost of base supporting electrolyte; $u_{r,n}$ and $u_{r,p}$ are the cost of negative and positive redox couples, respectively; $u_{se,n}$ and $u_{se,p}$ are the cost of negative and positive base supporting electrolytes, respectively.

For both negative and positive electrolytes, u_r and u_{se} are determined by the following equations.

$$u_r=P/(n\cdot W\cdot F);\ u_{se}=u_r/\Upsilon$$

where P is the chemical price, W is the molecular weight of chemical, and n is the number of working electrons/charges per molecule, F is Faraday's constant, Υ ratio of the concentration of redox pair to the concentration of corresponding base supporting.

The stack cost was calculated by the following equation, and the results are listed in Table S2.

$$U_s=U_{em}+U_m+U_b$$

where U_s is the stack cost, U_{em} is the cost of electrode materials, U_m is the cost of membrane and U_b is the bipolar plate cost.

Note that the membranes are self-made, we get the cost from our preparing process of PBI polymer, which includes the monomer cost, the electricity and even plus the personal costs. And the cost has been estimated in our previous report.(Yuan et al., 2016) The cost will be much lower as long as the mass production was realized. The bipolar plates we used are the same with our VFB system, which already

industrialized by our spin-off Dalian Rongke Power Co. Ltd,. And the cost is settled. The cost of Zn/Br, all vanadium and Fe/Cr flow battery systems were obtained from the reference.(Bruce Dunn et al., 2011) The cost of alkaline quinine flow battery was calculated according to the reference.(Gong et al., 2015) The cost of Fe/V flow battery system has already been reported.(Viswanathan et al., 2014) The practical output power density of a single cell was calculated according to the references.(Liu et al., 2016, Gong et al., 2015, Wang et al., 2011, Lopez-Atalaya et al., 1992, Wang et al., 2016, Lin et al., 2015)

References

Bruce Dunn, Haresh Kamath & Tarascon, J.-M. (2011). Electrical Energy Storage for the Grid: A Battery of Choices. Science 334, 928-935.

Chen, D., Yu, S., Liu, X. & Li, X. (2015). Porous polybenzimidazole membranes with excellent chemical stability and ion conductivity for direct borohydride fuel cells. J. Power Sources. 282, 323-327.

Dai, H, Zhang, H. M., Zhong, H. X., Jin, H., Li, X., Xiao, S., Mai, Z. (2010). Properties of polymer electrolyte membranes based on poly (aryl ether benzimidazole) and sulphonated poly (aryl ether benzimidazole) for high temperature PEMFCs. Fuel Cells. 10, 754-761.

Gong, K., Ma, X., Conforti, Kameron M., Kuttler, Kevin J., Grunewald, Jonathan B., Yeager, Kelsey L., Bazant, Martin Z., Gu, S., Yan, Y. (2015). A zinc–iron redox-flow battery under $100 per kW h of system capital cost. Energy Environ. Sci. 8, 2941-2945.

Lin, K. et al. (2015). Alkaline quinone flow battery. Science 349, 1529-1532.

Liu, T., Wei, X., Nie, Z., Sprenkle, V. & Wang, W. (2016). A Total Organic Aqueous Redox Flow Battery Employing a Low Cost and Sustainable Methyl Viologen Anolyte and 4-HO-TEMPO Catholyte. Adv. Energy Mater. 6, 1501449.

Lopez-Atalaya, M., Codina, G., Perez, J. R., Vazquez, J. L. & Aldaz, A. (1992). Optimization studies on a Fe/Cr redox flow battery. J. Power Sources. 39, 147-154.

Shah, A. A., Tangirala, R., Singh, R., Wills, R. G. A. & Walsh, F. C. (2011). A Dynamic Unit Cell Model for the All-Vanadium Flow Battery. J. Electrochem. Soc. 158, A671-A677.

Viswanathan, V. et al. (2014). Cost and performance model for redox flow batteries. J. Power Sources. 247, 1040-1051.

Wang, C., Li, X., Xi, X., Zhou, W., Lai, Q., Zhang, H. M. (2016). Bimodal highly ordered mesostructure carbon with high activity for Br2/Br− redox couple in bromine

based batteries. Nano Energy 21, 217-227.
Wang, W., Kim, Soowhan, Chen, B., Nie, Z., Zhang, J., Xia, G., Li, L., Yang, Z. (2011). A new redox flow battery using Fe/V redox couples in chloride supporting electrolyte. Energy Environ. Sci. 4, 4068-4073.
Yuan, Z., Duan, Y., Zhang, H., Li, X., Zhang, H. M., Vankelecom, Ivo. (2016). Advanced porous membranes with ultra-high selectivity and stability for vanadium flow batteries. Energy Environ. Sci. 9, 441-447.

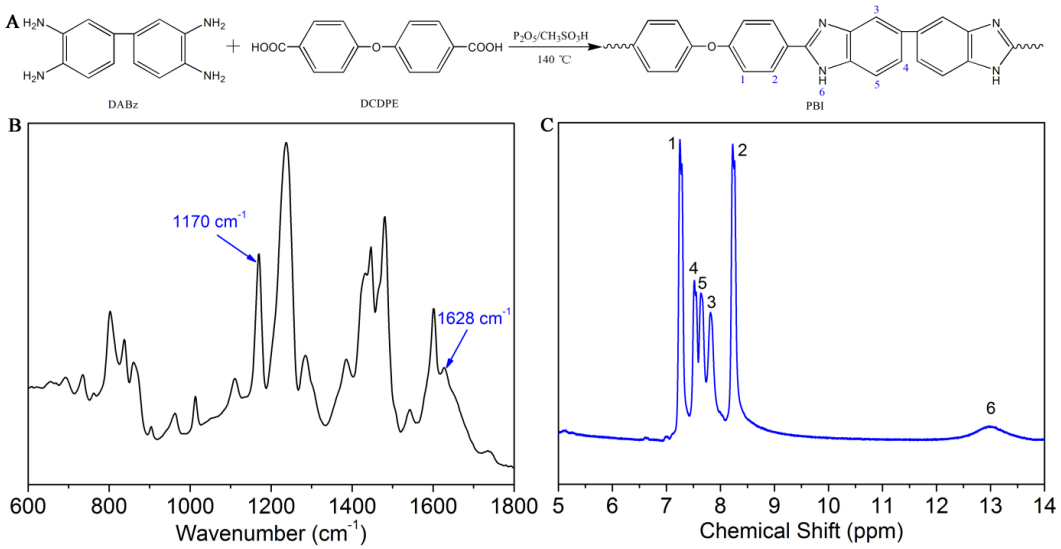

Figure S1 Polybenzimidazole (PBI) polymer synthesis and characterization, Related to Figure 1, Figure 2, Figure 3 and Figure 4.

(A) The synthesis of PBI. (B) The FTIR spectrum of PBI. (C) The ^{1}H NMR spectrum of PBI.

The absorption band at 1170 cm^{-1} is attributed to the stretch vibration of C-O-C. The absorption band at 1628 cm^{-1} is the stretch vibration of C=N and C=C. The absorption bands ranging from 2500 to 3500 cm^{-1} are attributed to the N-H group in the imidazole ring, while the absorption band at around 3400 cm^{-1} is derived from the stretch vibration of the isolated non-hydrogen bonded N-H group.

^{1}H NMR δ = 7.25 (2H, s), 7.54 (1H, J=12.8, d), 7.65 (1H, s), 7.82 (1H, s), 8.23 (2H, s), 12.99 (1H, s). H1 and H2 are the hydrogens of the benzene ring next to the ether bond. H3, H4 and H5 are the benzene hydrogen in the benzimidazole ring. The H6 peak is the hydrogen of the imidazole ring, with a chemical shift at 12.99 ppm. The FTIR and ^{1}H NMR spectrum thus confirm the expected structure of PBI.

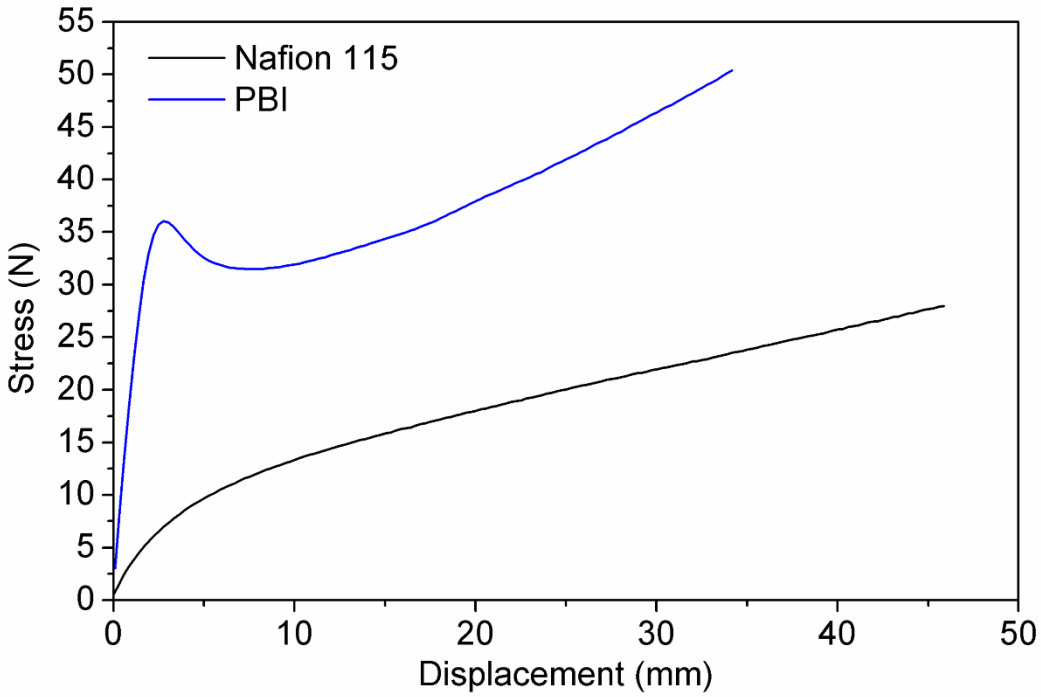

Membrane	Elasticity modulus (MPa)	Elongation at break (%)	Tensile breaking stress (MPa)	Tensile strength (MPa)
Nafion 115	93.7	92.22	19.39	19.39
PBI	2953.01	68.5	137.31	137.31

Figure S2 Mechanical properties of PBI and Nafion 115 membranes, Related to Figure 1.

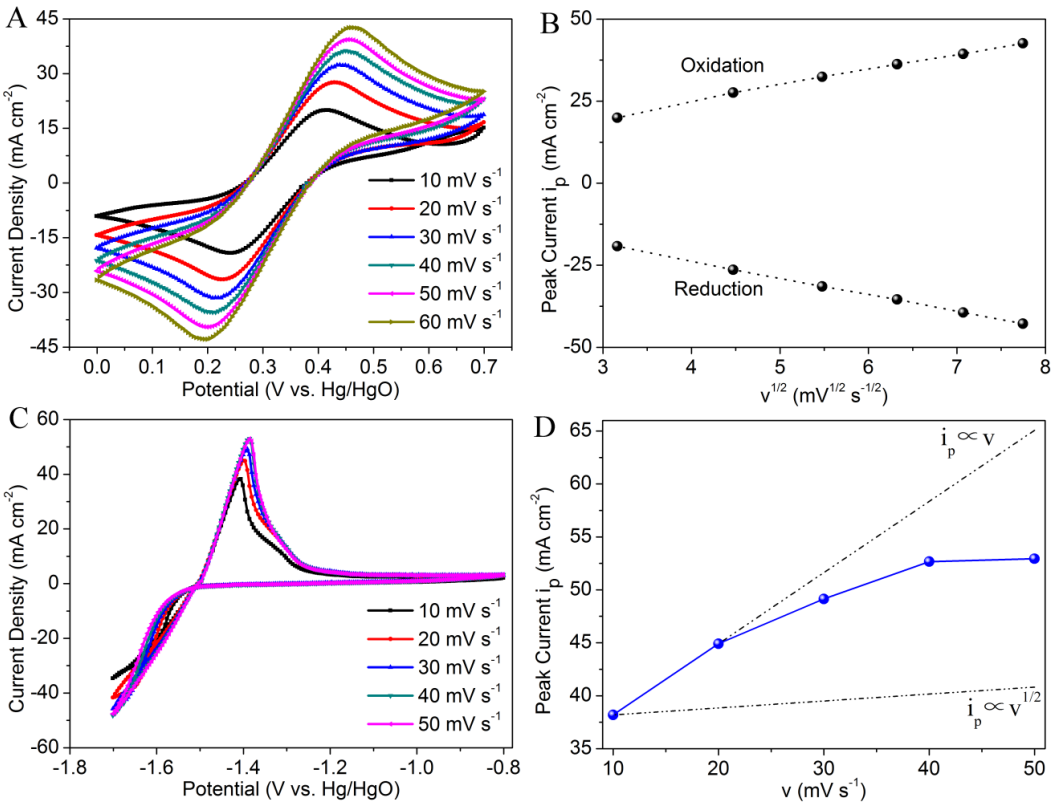

Figure S3 Cyclic voltammetry of $Fe(CN)_6^{3-}/Fe(CN)_6^{4-}$ and $Zn(OH)_4^{2-}/Zn$ redox couples, Related to Figure 1.

(A) CV scans of 0.2 mol L^{-1} $K_3Fe(CN)_6$ + 0.2 mol L^{-1} $K_4Fe(CN)_6$ in 3 mol L^{-1} sodium hydroxide solution at different sweeping rates. (B) Linear relationships between the oxidation and reduction peak current densities with the square root of the sweeping rate. (C) CV scans of 0.1 mol L^{-1} $Zn(OH)_4^{2-}$ in 3 mol L^{-1} sodium hydroxide solution at different sweeping rates. (D) The relationship between the oxidation peak current density with the square root of the sweeping rate.

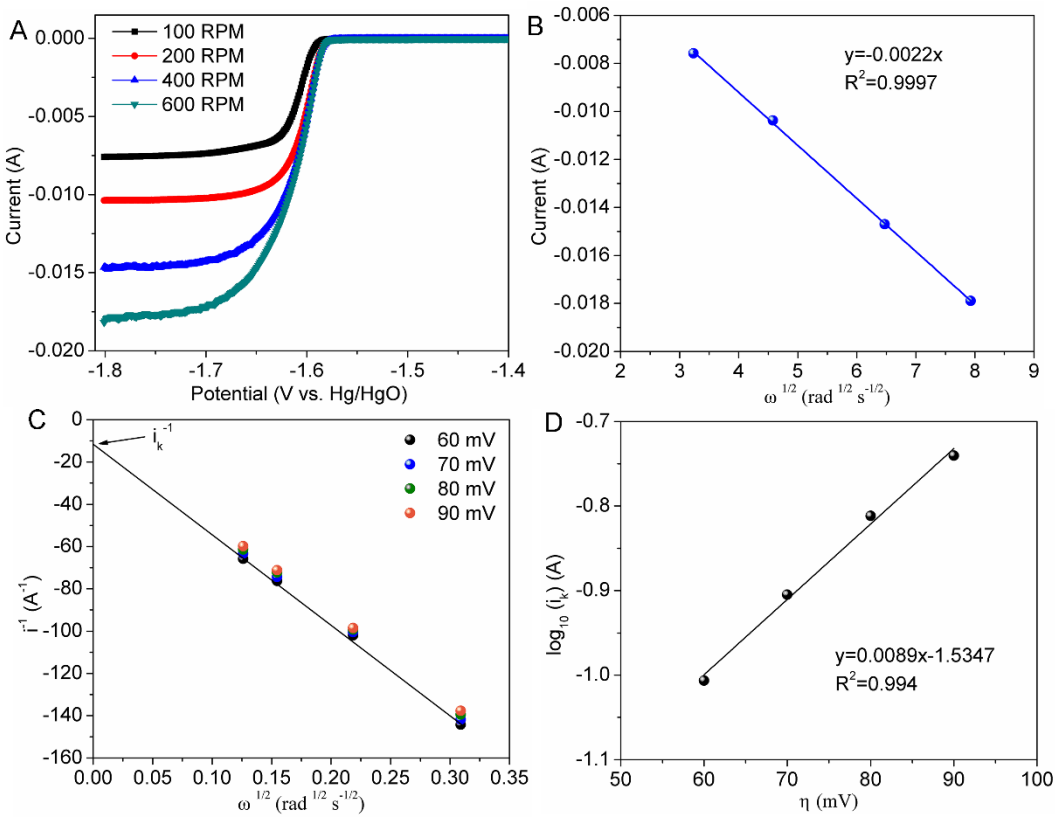

Figure S4 Electrochemistry of $Zn(OH)_4^{2-}$ deposition on a glassy carbon electrode, Related to Figure 1.

(A) Rotating disk electrode measurements at rotating electrode speeds from 100 to 600 RPM using 0.2 mol L^{-1} $Zn(OH)_4^{2-}$ in 3 mol L^{-1} sodium hydroxide solution. (B) Linear relationships between the limiting current and the square root of the rotation velocity (Levich-plot). (C) Koutecky´–Levich plot. (D) Tafel plot.

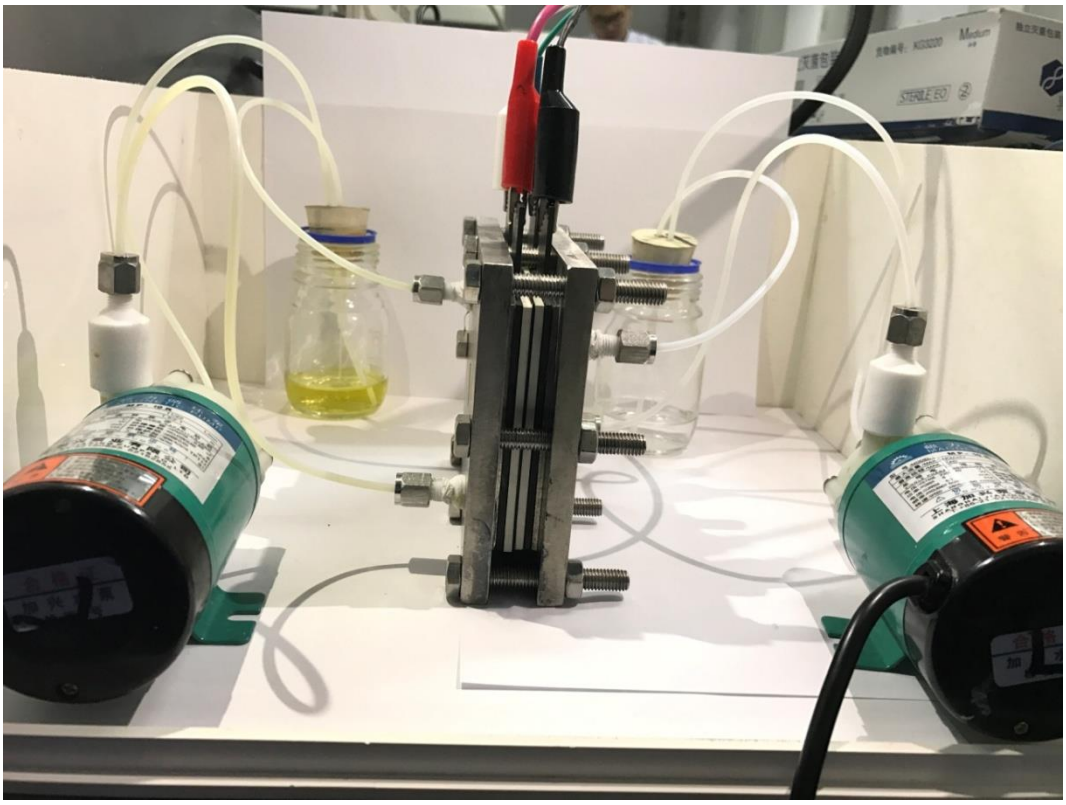

Figure S5 The prototype of an alkaline zinc-iron flow battery using a self-made, low cost non-fluorinated ion exchange membrane. The active area of the electrode is 48 cm^2, Related to Figure 2.

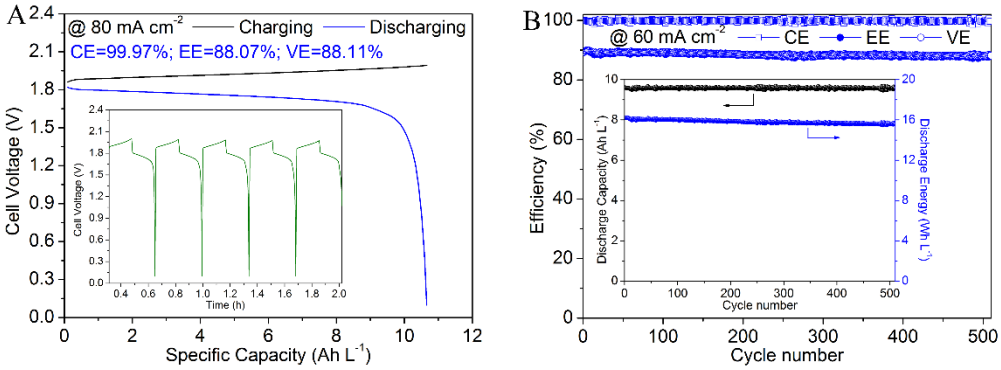

Figure S6 Battery performance of the alkaline zinc-iron flow battery assembled with a self-made PBI membrane, Related to Figure 2.

(A) Cell voltage profile of the alkaline zinc-iron flow battery with self-made PBI membrane at a current density of 80 mA cm^{-2}. Insert, charge and discharge curves. (B) Long-term stability of the alkaline zinc-iron flow battery with a PBI membrane at a current density of 60 mA cm^{-2}. Inserts, discharge capacity and discharge energy during the cycling stability experiment. 60 mL 0.6 mol L^{-1} $K_4Fe(CN)_6$ + 5 mol L^{-1} sodium hydroxide solution and 60 mL 0.3 mol L^{-1} $Zn(OH)_4^{2-}$ + 5 mol L^{-1} sodium hydroxide solution were used in positive and negative electrolyte, respectively. The charge process was controlled by the charge time to keep a constant charge capacity, while the discharge process was ended with the cut-off voltage of 0.1 V.

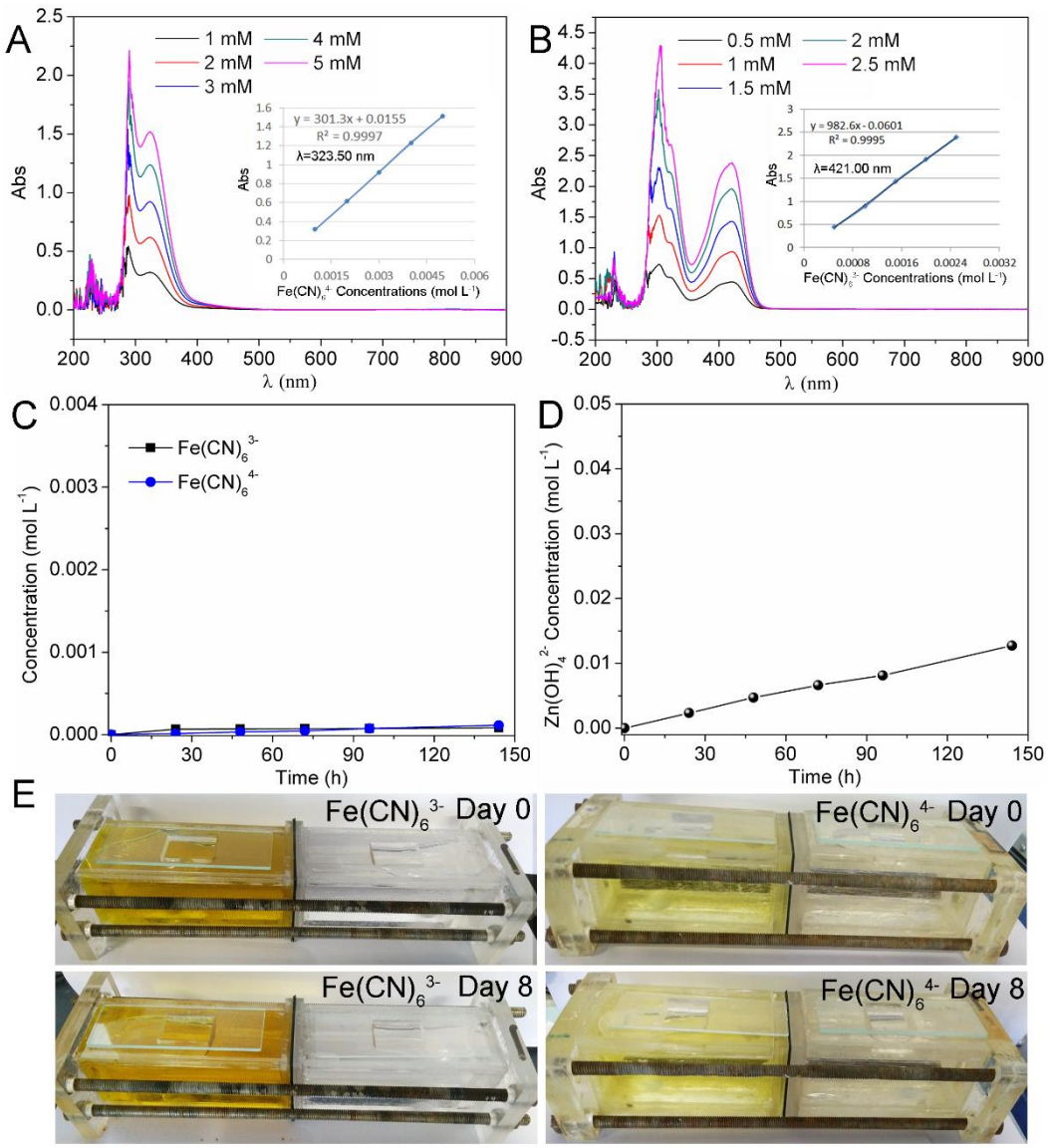

Figure S7 Permeability experiment of anionic active species through the PBI membrane, Related to Figure 2 and Figure 3.

(A) UV-vis absorption spectrum of different concentrations of $Fe(CN)_6^{4-}$ in 3 M NaOH solutions (Inserts: standard curve of $Fe(CN)_6^{4-}$ concentration *vs.* Abs at λ=323.50 nm). (B) UV-vis absorption spectrum of different concentrations of $Fe(CN)_6^{3-}$ in 3 M NaOH solutions (Inserts: standard curve of $Fe(CN)_6^{3-}$ concentration *vs.* Abs at λ=421 nm). (C) $Fe(CN)_6^{3-}$/$Fe(CN)_6^{4-}$ concentration versus time at the diffused side of a diffusion cell using PBI membrane (detected by the UV-Visible spectroscopy). (D) $Zn(OH)_4^{2-}$ concentration versus time at the diffused side of a diffusion cell using PBI membrane (detected by the inductively coupled plasma mass spectrometry, ICP-MS). (E) Visual experimental of $Fe(CN)_6^{3-}$/$Fe(CN)_6^{4-}$ permeability. From the diffused side of the diffusion cell, no obviously color change could be observed, demonstrating high selectivity of the PBI membrane.

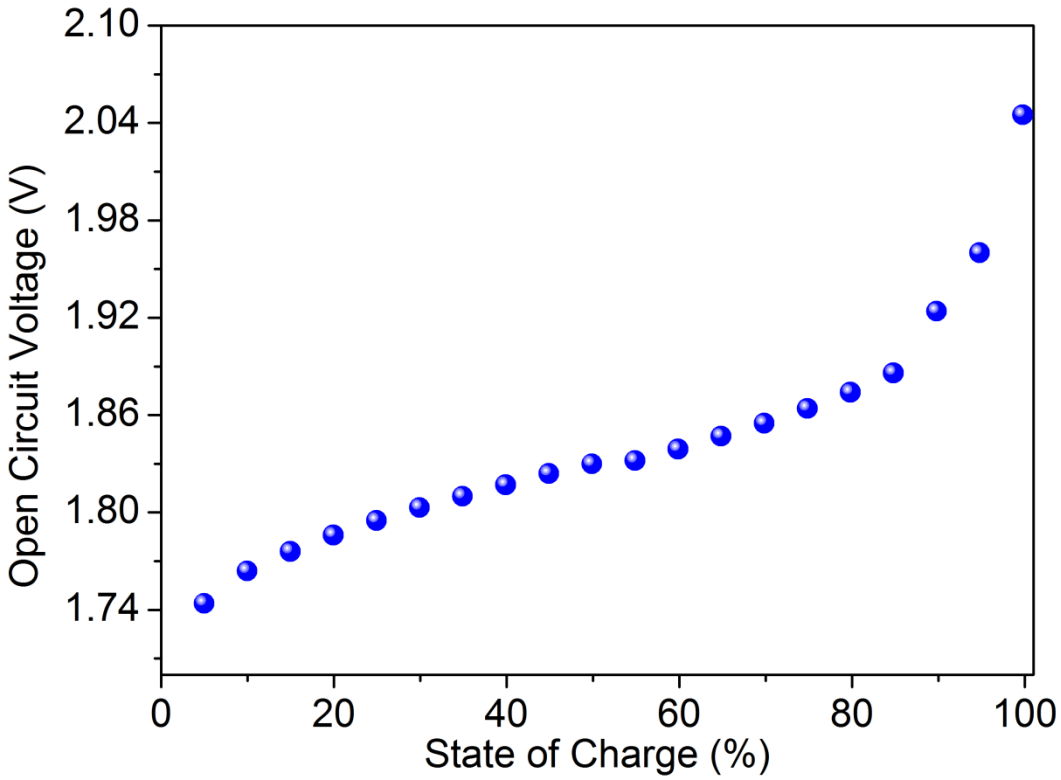

Figure S8 The open cell voltage versus state of charge of an alkaline zinc-iron flow battery, Related to Figure 1, Figure 2 and Figure 3.

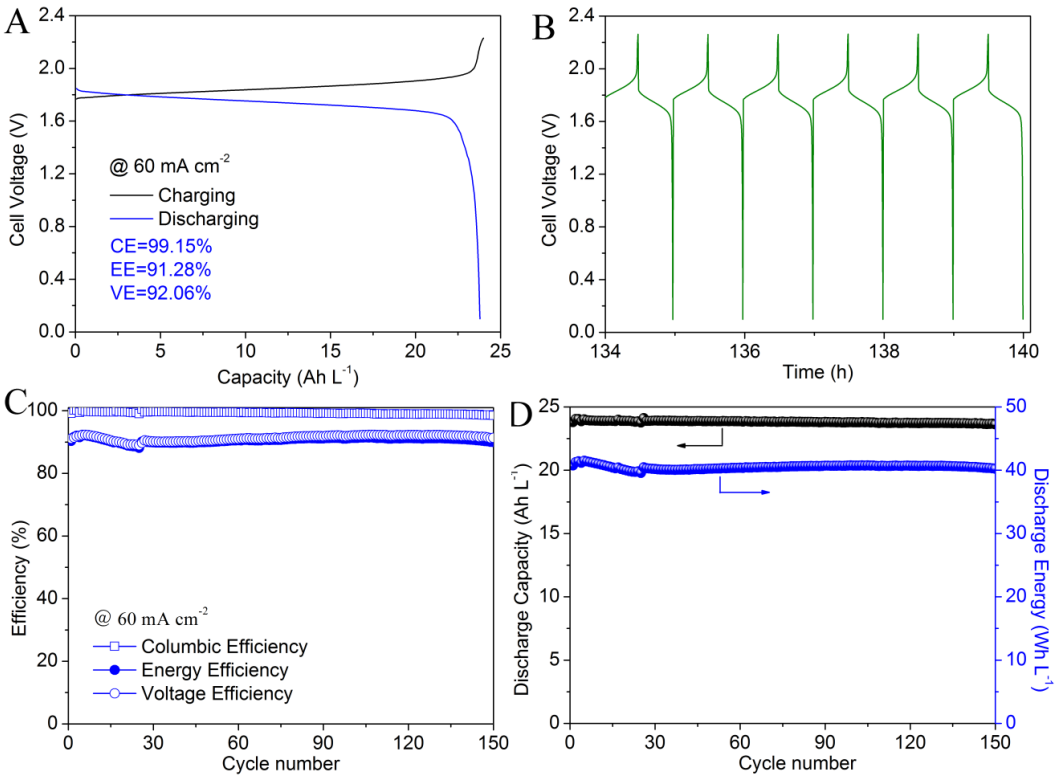

Figure S9 Battery performance of an alkaline zinc-iron flow battery at the current density of 60 mA cm^{-2}, Related to Figure 1 and Figure 2.

(A) Cell voltage profile of the alkaline zinc-iron flow battery with a self-made ion exchange membrane at the current density of 60 mA cm^{-2}. (B) Parts of charge and discharge cycles of the alkaline zinc-iron flow battery. (C) Long-term stability of alkaline zinc-iron flow battery, remaining a stable coulombic efficiency above 99%, an energy efficiency above 90% after 150 charging and discharging cycles at the current density of 60 mA cm^{-2}. (D) Discharge capacity and discharge energy of each cycle in the same 150 charging and discharging cycles of alkaline zinc-iron flow battery. 60 mL 1.0 mol L^{-1} $Na_4Fe(CN)_6$ + 3 mol L^{-1} potassium hydroxide solution and 60 mL 0.5 mol L^{-1} $Zn(OH)_4^{2-}$ + 4 mol L^{-1} sodium hydroxide solution were used in positive and negative electrolyte, respectively.

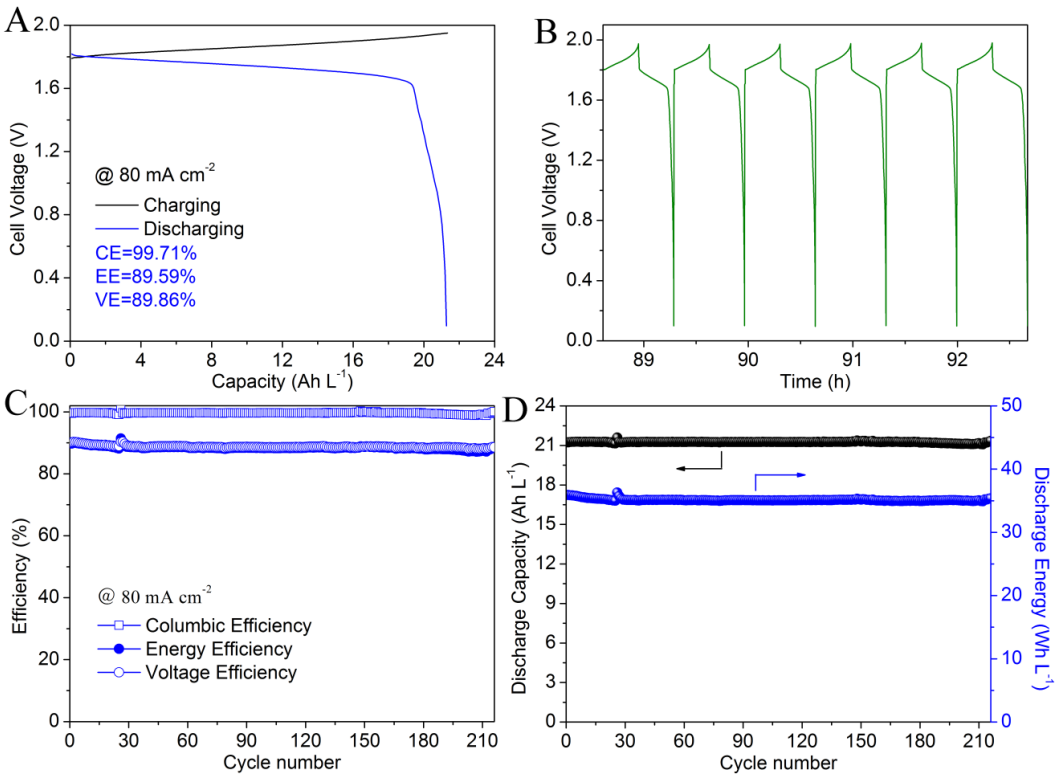

Figure S10 Battery performance of an alkaline zinc-iron flow battery at the current density of 80 mA cm^{-2}, Related to Figure 1 and Figure 2.

(A) Cell voltage profile of the alkaline zinc-iron flow battery with a self-made ion exchange membrane at the current density of 80 mA cm^{-2}. (B) Parts of charge and discharge cycles of the alkaline zinc-iron flow battery. (C) Long-term stability of the alkaline zinc-iron flow battery at the current density of 80 mA cm^{-2}. (D) Discharge capacity and discharge energy of each cycle in the same 210 charging and discharging cycles of alkaline zinc-iron flow battery. 60 mL 1.0 mol L^{-1} $Na_4Fe(CN)_6$ + 3 mol L^{-1} potassium hydroxide solution and 60 mL 0.5 mol L^{-1} $Zn(OH)_4^{2-}$ + 4 mol L^{-1} sodium hydroxide solution were used in positive and negative electrolyte, respectively.

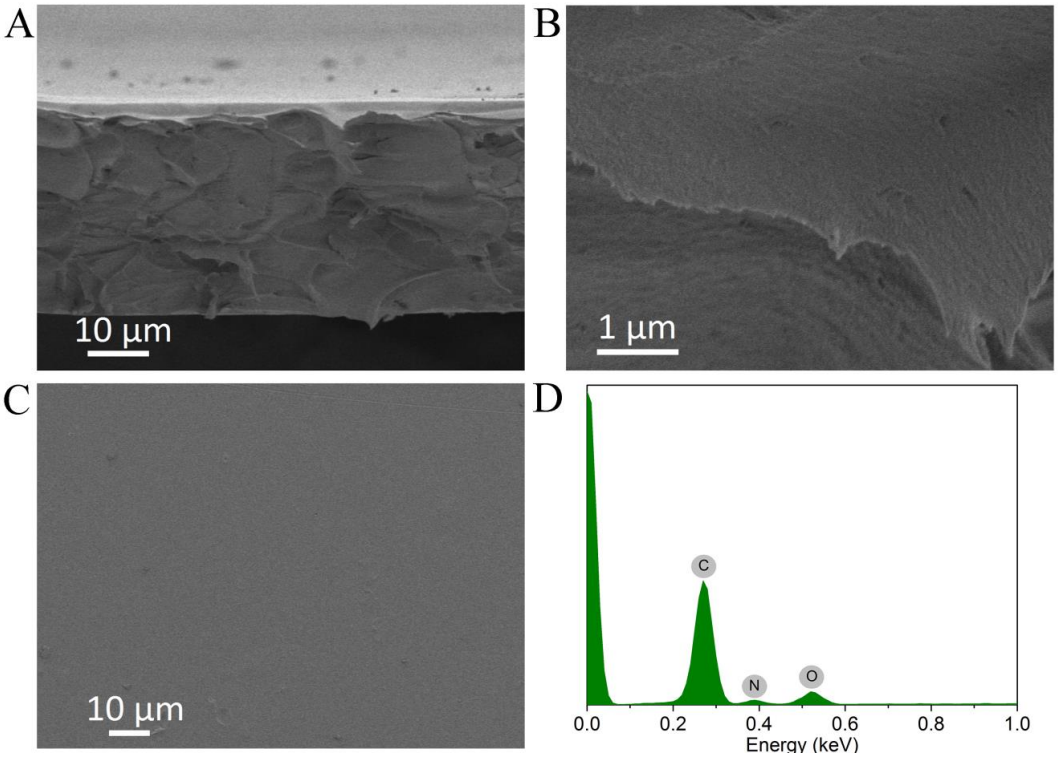

Figure S11 Cross section and surface morphologies of the self-made PBI membranes, Related to Figure 1 and Figure 4.

(A) Cross section and (B) magnified cross section morphologies of the PBI membrane. (C) Surface morphology of the PBI membrane. (D) The EDS spectrum of PBI membrane surface.

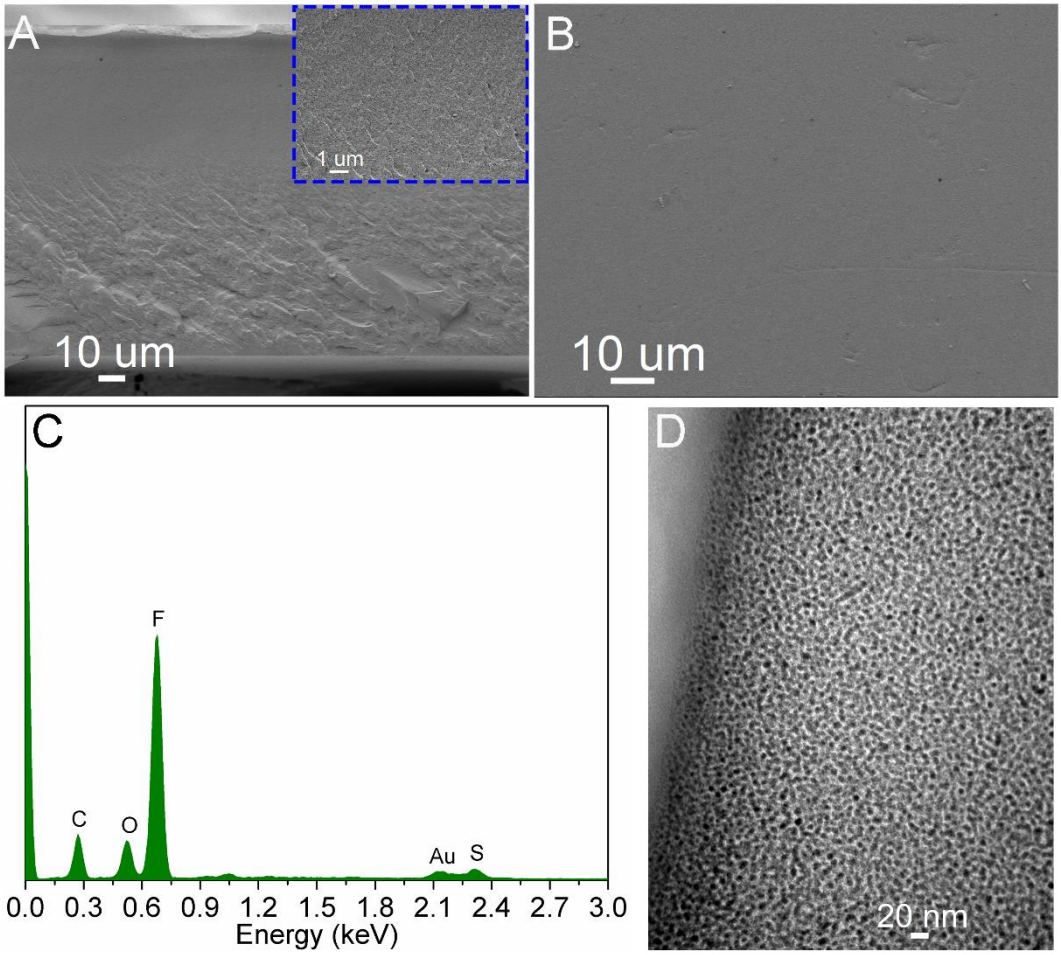

Figure S12 Morphologies and elemental composition of the Nafion 115 membrane, Related to Figure 1 and Figure 5.

(A) Cross section (inserts: magnified cross section morphology) morphology of the Nafion 115 membrane. (B) Surface morphology of the Nafion 115 membrane. (C) The EDS spectrum of Nafion 115 membrane cross section. (D) Morphology of hydrophilic domain of Nafion 115 recorded by TEM.

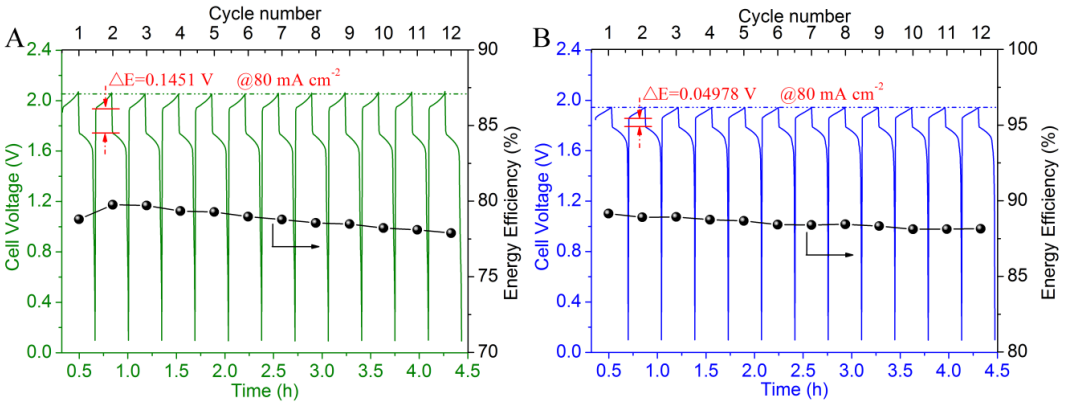

Figure S13 Battery performance of the alkaline zinc-iron flow battery assembled with a self-made PBI and a Nafion 115 membrane. Related to Figure 1 and Figure 2.

(A) Cell voltage profile and energy efficiency of an alkaline zinc-iron flow battery with a Nafion 115 membrane at the current density of 80 mA cm^{-2}. (B) Cell voltage profile and energy efficiency of an alkaline zinc-iron flow battery with a self-made PBI membrane at the current density of 80 mA cm^{-2}. 60 mL 0.6 mol L^{-1} $K_4Fe(CN)_6$ + 5 mol L^{-1} sodium hydroxide solution and 60 mL 0.3 mol L^{-1} $Zn(OH)_4^{2-}$ + 5 mol L^{-1} sodium hydroxide solution were used in positive and negative electrolyte, respectively. The charge process was controlled by the charge time to keep a constant charge capacity, while the discharge process was ended with the cut-off voltage of 0.1 V.

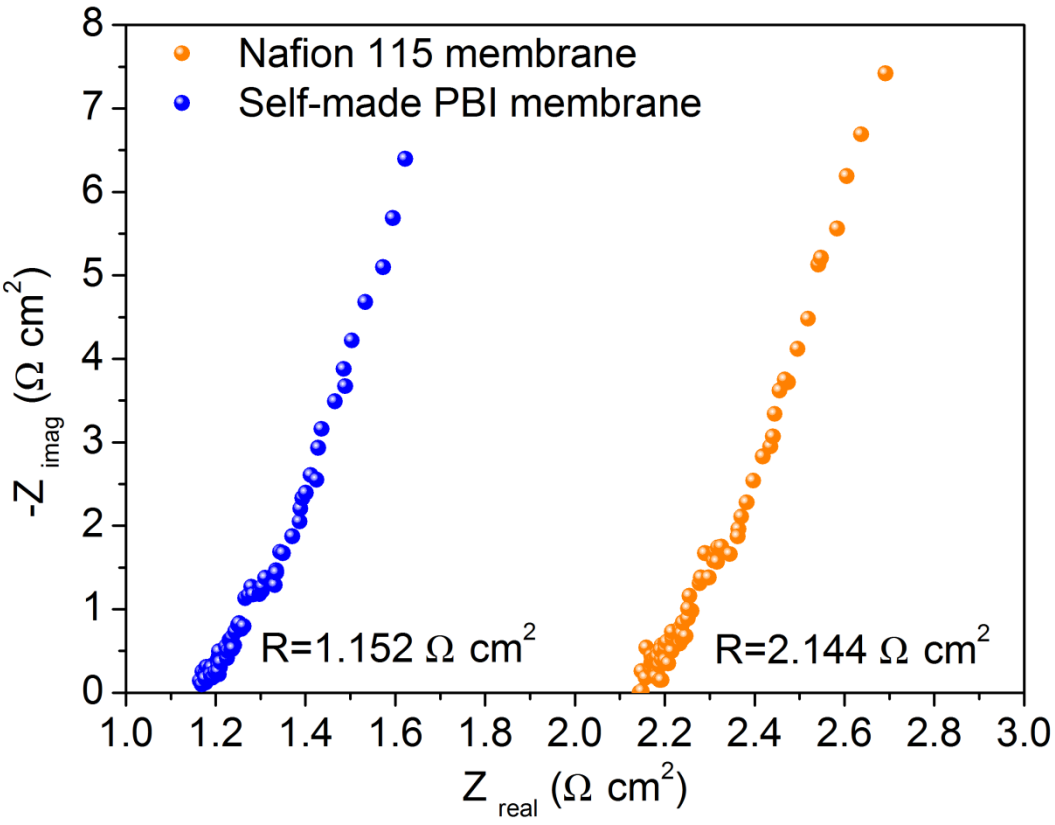

Figure S14 Nyquist plots of the alkaline zinc-iron flow batteries with a self-made membrane and a Nafion 115 membrane, Related to Figure 1, Figure 2 and Figure 3.

The experiments were conducted at 50% SOC. From the Nyquist plots, we can only find a linear region at low frequencies, which attributes to the ohmic resistance of the membrane. We cannot observe the semicircle (charge transfer process) at high frequencies since the kinetics of $Zn(OH)_4^{2-}/Zn$ and $Fe(CN)_6^{3-}/Fe(CN)_6^{4-}$ are very fast on the carbon felt electrode.

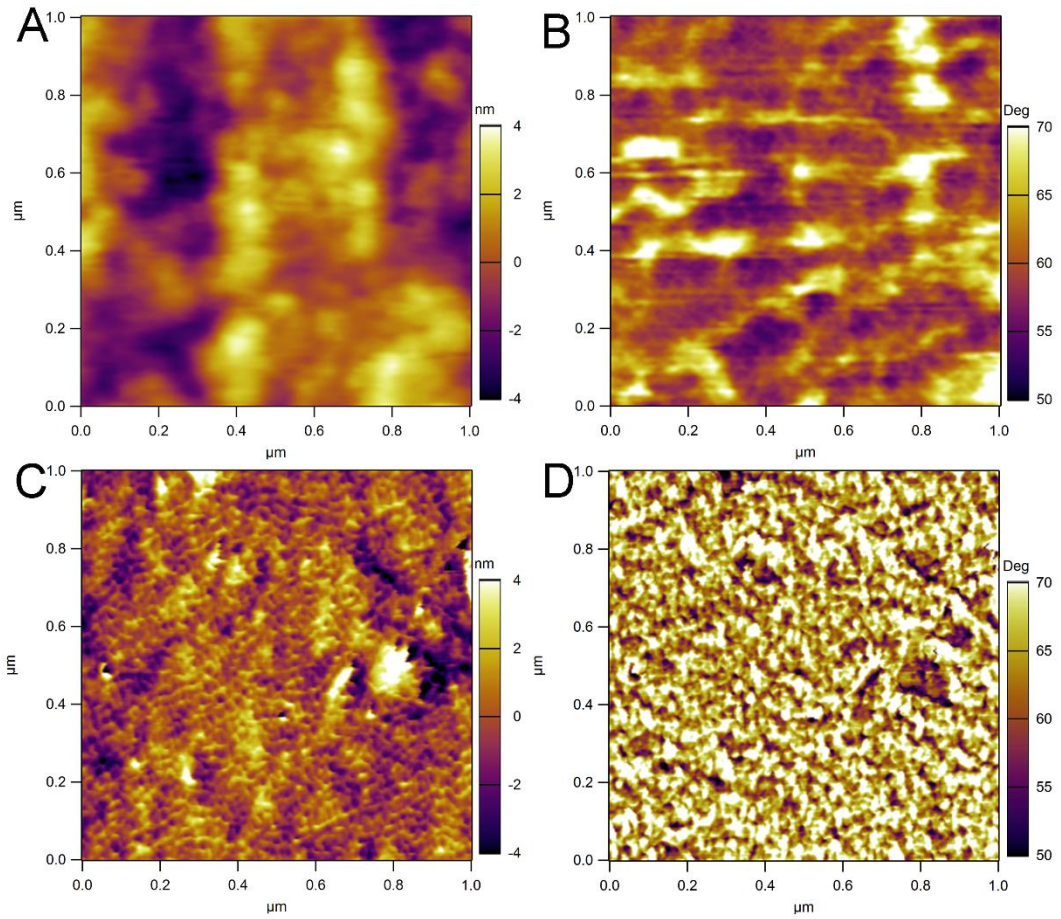

Figure S15 Atomic force microscope morphologies of the Nafion 115 and PBI membranes, Related to Figure 1.

(A) Surface topography contrast image of Nafion 115 membrane. (B) Surface phase contrast image of Nafion 115 membrane. (C) Surface topography contrast image of PBI membrane. (D) Surface phase contrast image of PBI membrane.

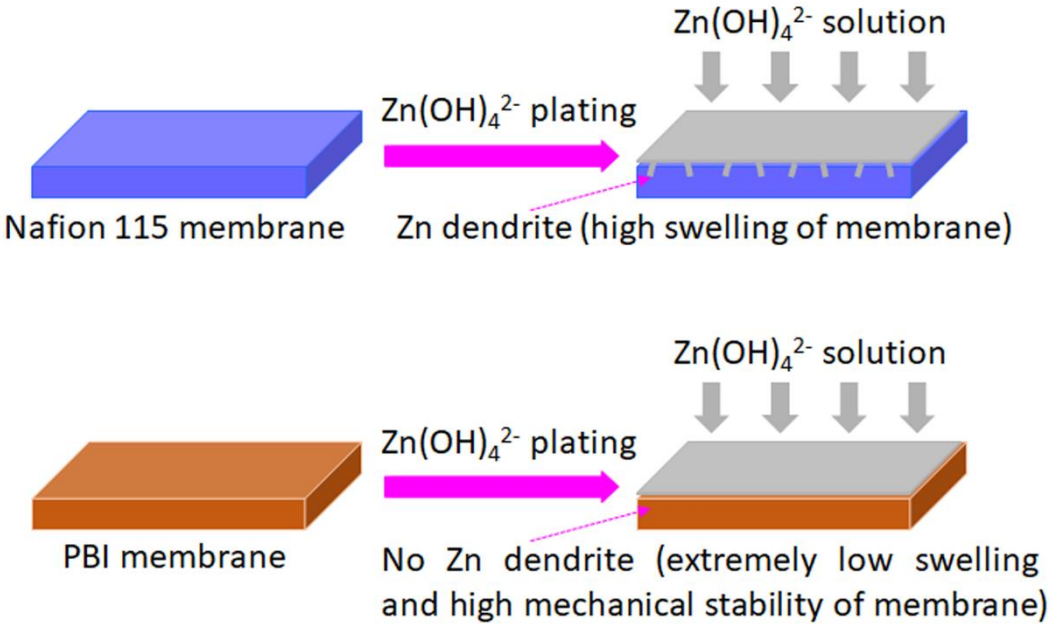

Figure S16 Schematic diagrams of $Zn(OH)_4^{2-}$ plating behavior for an alkaline zinc-iron flow battery using a Nafion 115 and PBI membranes, Related to Figure 1.

Zinc dendrites grow into Nafion 115 membrane during $Zn(OH)_4^{2-}$ plating process since the swelling of Nafion 115 membrane is high and its low mechanical stability. By contrast, zinc dendrites cannot grow into PBI membrane during $Zn(OH)_4^{2-}$ plating process since the swelling of PBI membrane is extremely low and its ultrahigh mechanical stability.

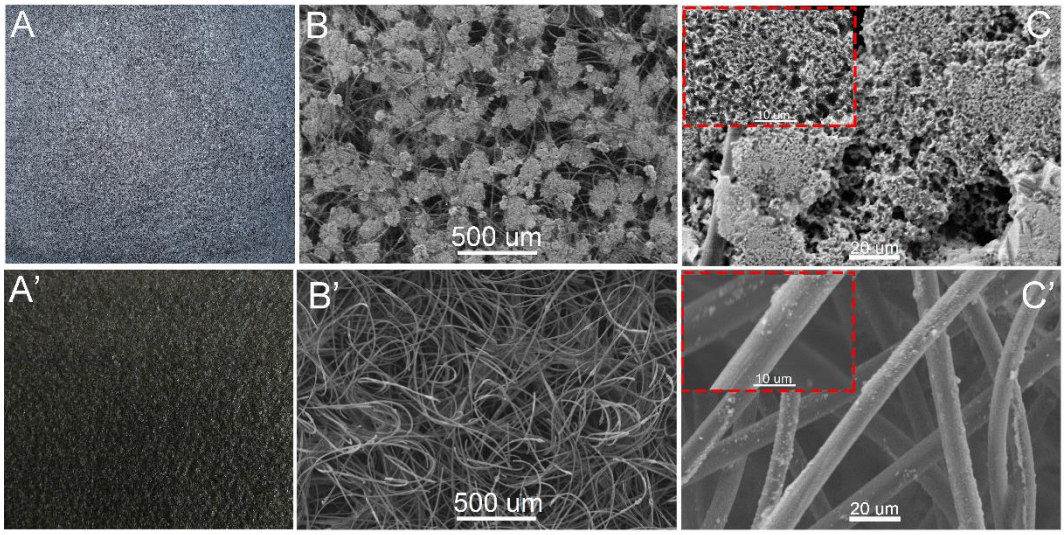

Figure S17 Morphologies of the negative electrode before and after cycling test using a PBI membrane, Related to Figure 2.

Optical image of the negative electrode for the alkaline zinc-iron flow battery after charge (A) and discharge (A') cycle tests at 80 mA cm^{-2}; SEM images of surface morphology on the negative electrode after charge (B) and discharge (B') cycle tests at 80 mA cm^{-2}; Magnified SEM images of surface morphology on the negative electrode after charge (C) and discharge (C') cycle tests at 80 mA cm^{-2}. 60 mL 1.0 mol L^{-1} $Na_4Fe(CN)_6$ + 3 mol L^{-1} potassium hydroxide solution and 60 mL 0.5 mol L^{-1} $Zn(OH)_4^{2-}$ + 4 mol L^{-1} sodium hydroxide solution were used in positive and negative electrolyte, respectively. The charge process was controlled by the charge time (20 minutes) to keep a constant charge capacity, while the discharge process was ended with the cut-off voltage of 0.1 V.

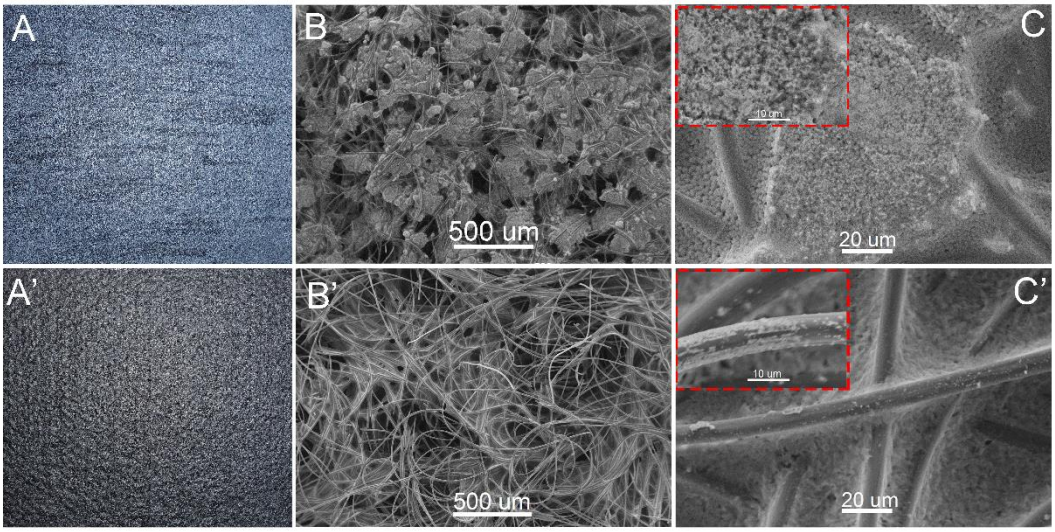

Figure S18 Morphologies of the negative electrode before and after cycling test using a Nafion 115 membrane, Related to Figure 1.

Optical image of the negative electrode for the alkaline zinc-iron flow battery after charge (A) and discharge (A') cycle tests at 80 mA cm^{-2}; SEM images of surface morphology on the negative electrode after charge (B) and discharge (B') cycle tests at 80 mA cm^{-2}; Magnified SEM images of surface morphology on the negative electrode after charge (C) and discharge (C') cycle tests at 80 mA cm^{-2}. 60 mL 1.0 mol L^{-1} $Na_4Fe(CN)_6$ + 3 mol L^{-1} potassium hydroxide solution and 60 mL 0.5 mol L^{-1} $Zn(OH)_4^{2-}$ + 4 mol L^{-1} sodium hydroxide solution were used in positive and negative electrolyte, respectively. The charge process was controlled by the charge time (20 minutes) to keep a constant charge capacity, while the discharge process was ended with the cut-off voltage of 0.1 V.

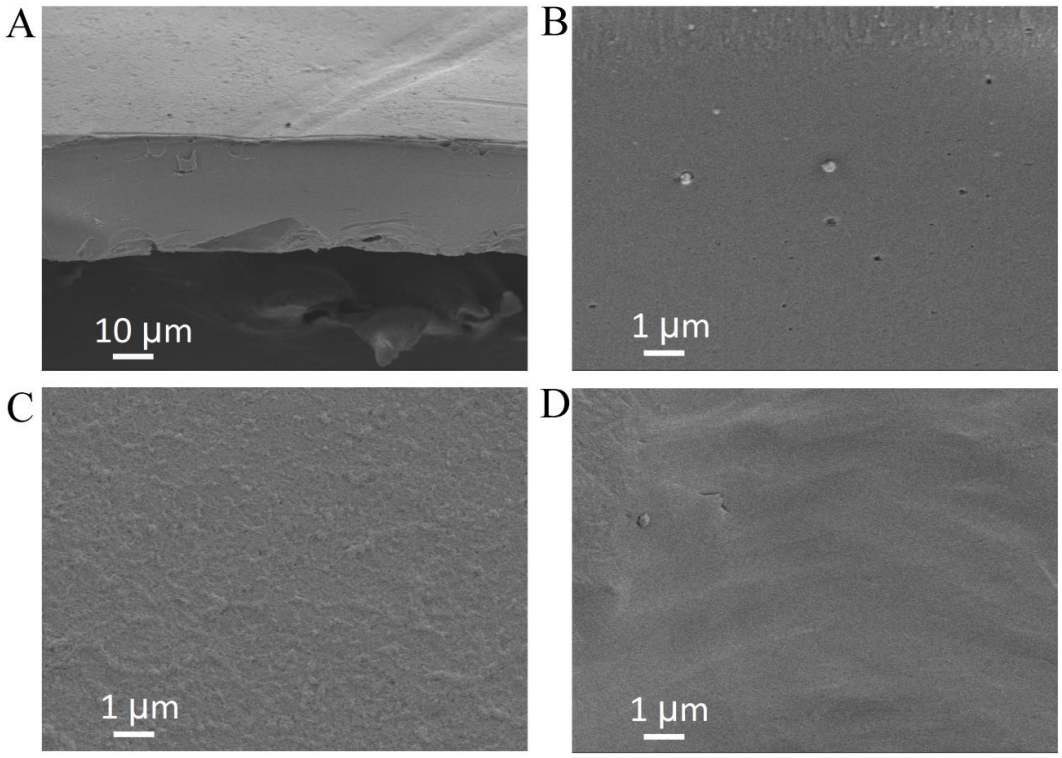

Figure S19 Morphologies of the self-made PBI membrane after the stability test, Related to Figure 3.

(A) Cross section and (B) magnified cross section morphologies of the PBI membrane. (C) Surface morphology of the PBI membrane facing the negative side. (D) Surface morphology of the PBI membrane toward the positive side.

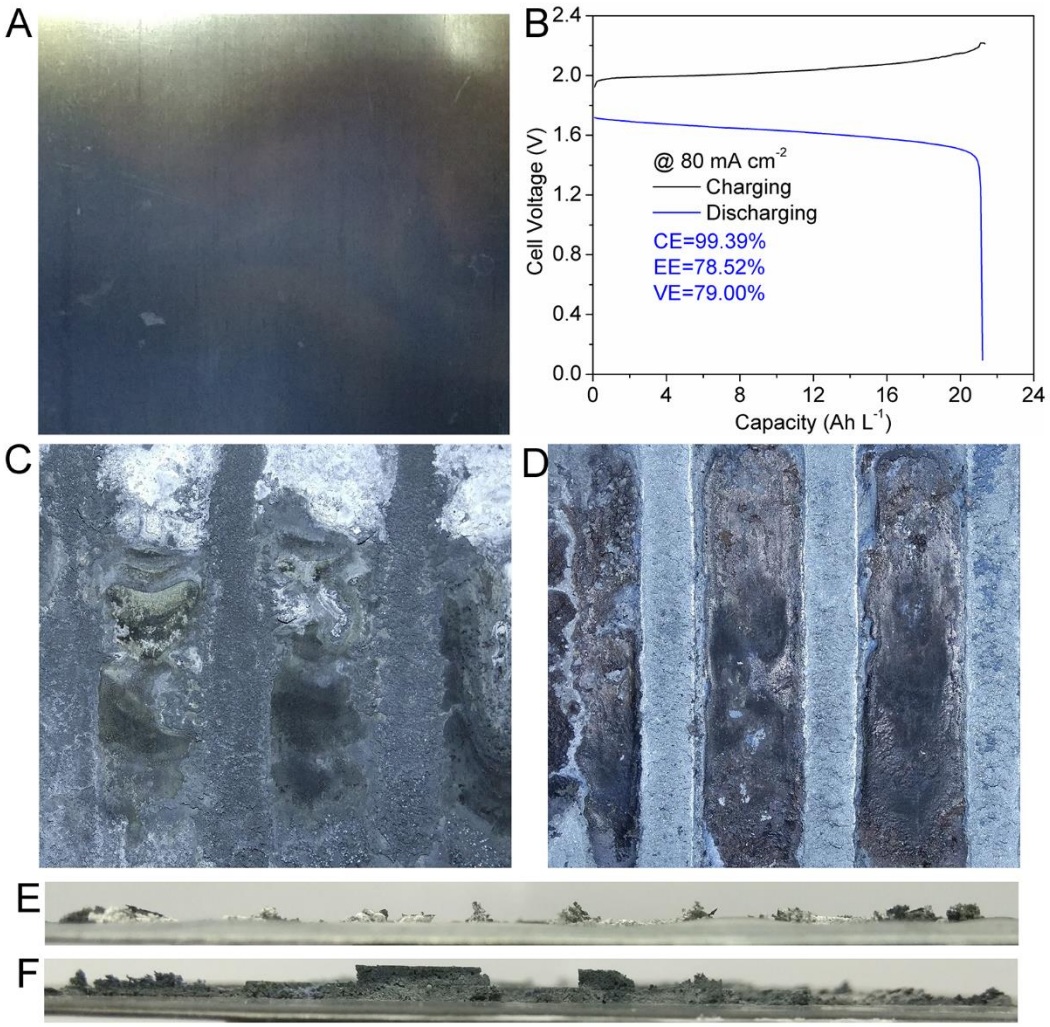

Figure S20 An alkaline zinc-iron flow battery using a zinc plate as electrode, Related to Figure 1.

(A) Optical image of the zinc plate electrode. (B) Cell voltage profile of the alkaline zinc-iron flow battery with a PBI membrane by using a zinc plate as the electrode at the current density of 80 mA cm^{-2}. (C) Optical image of the zinc plate electrode at the end of charging (top view). (D) Optical image of the zinc plate electrode at the end of discharging (top view). (E) Optical image of the zinc plate electrode at the end of charging (cross section view). (F) Optical image of the zinc plate electrode at the end of discharging (cross section view). 60 mL 1.0 mol L^{-1} $Na_4Fe(CN)_6$ + 3 mol L^{-1} potassium hydroxide solution and 60 mL 0.5 mol L^{-1} $Zn(OH)_4^{2-}$ + 4 mol L^{-1} sodium hydroxide solution were used in positive and negative electrolyte, respectively.

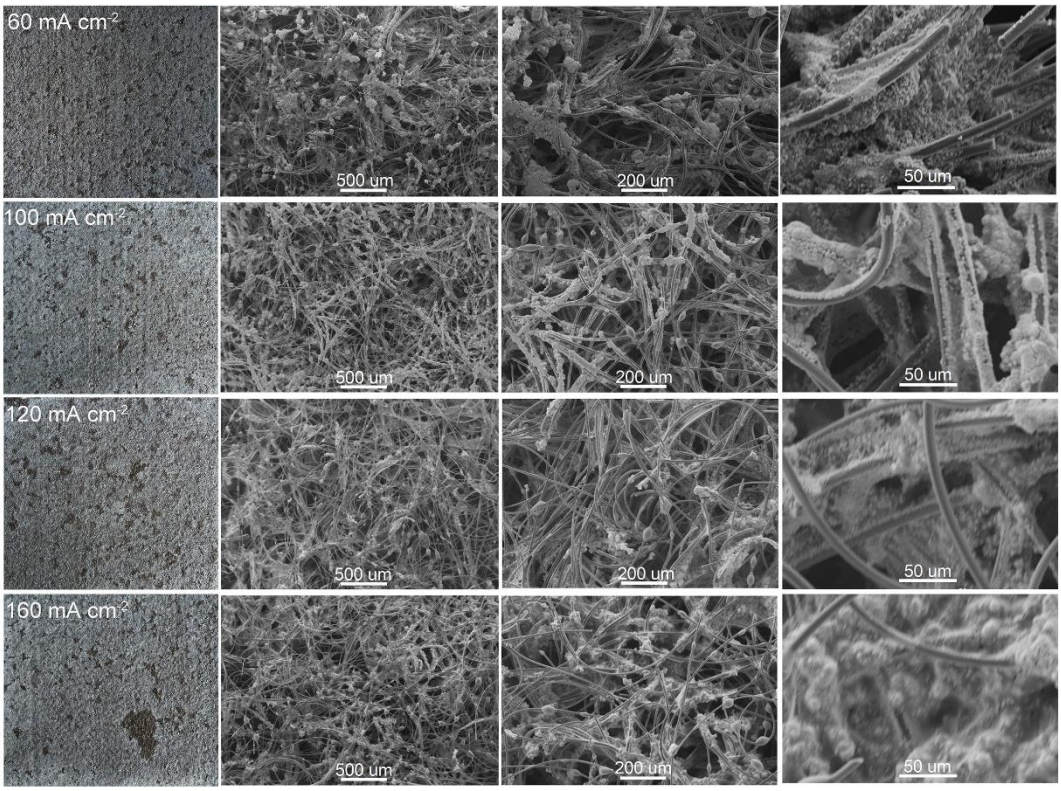

Figure S21 Morphologies of zinc deposition with current density ranging from 60 mA cm^{-2} to 160 mA cm^{-2}, Related to Figure 1 and Figure 2.

Table S1 Electrolyte cost for alkaline zinc-iron flow battery, Related to Figure 5.

Flow Battery	U_r (¢/Ah)[a]	U_{ss} (¢/Ah)[b]	U_e (¢/Ah)[c]
Alkaline zinc-iron flow battery	2.1	0.83	2.93

[a] The cost information and detailed calculation are shown in Table S3

[b] The cost information and detailed calculation are shown in Table S4

[c] The U_e stands for unit electrolyte price of full battery. The electrolyte cost at standard cell voltage is calculated as $C_e=U_e/V_{rev}$.

Table S2 Stack cost for alkaline zinc-iron flow battery, Related to Figure 5.

Flow Battery	U_{em} ($/m^2)[a]	U_m ($/m^2)[a]	U_b ($/m^2)[b]	U_s($/m^2)
Alkaline zinc-iron flow battery	118	40	12	170

[a] Detailed calculation is shown in Table S5 and Table S6; [b] The bipolar plate is self-made.

Table S3 Prices of redox compounds, Related to Figure 5.

Compound	Molecular weight (W) (g/mol)	Price (P) ($/kg)	n	u_r (¢/Ah)
ZnO	81.39	1.3[a]	2	0.2
$Na_4Fe(CN)_6\cdot10H_2O$	484.06	1.07[b]	1	1.9

[a] From reference (Gong et al., 2015); [b] Quoted from Jinan Dehou Chemical Co., Ltd.

Table S4 Prices of supporting base, Related to Figure 5.

Chemical	Molecular weight (W) (g/mol)	Price (P) ($/kg)	n	ϒ	u_{ss} (¢/Ah)
NaOH	40.00	0.4[a]	2	0.1	0.3
KOH	56.11	0.84[b]	1	0.33	0.53

[a] From reference (Gong et al., 2015); [b] Quoted from Jinan Li Yang Chemical Co., Ltd.

Table S5 Prices of electrode materials, Related to Figure 5.

Electrode materials	Price
Carbon felt ($ m^{-2})	70[a]
Copper mesh	48[a]

[a] From reference (Gong et al., 2015)

Table S6 Prices of membrane materials, Related to Figure 5.

Membranes	Price
Self-made PBI membrane ($ m^{-2})	40[a]

[a] The PBI membrane is self-made.